Supplementary Information

# Subnanometric alkaline-earth oxide clusters for sustainable nitrate to ammonia photosynthesis

**Jieyuan Li,[1,2] Ruimin Chen,[1] Jielin Wang,[1] Ying Zhou,[3] Guidong Yang,[4] Fan Dong[1,2*]**

1 Research Center for Environmental and Energy Catalysis, Institute of Fundamental and Frontier Sciences, University of Electronic Science and Technology of China, Chengdu 611731, China.

2 Yangtze Delta Region Institute (Huzhou), University of Electronic Science and Technology of China, Huzhou 313000, China.

3 School of New Energy and Materials, Southwest Petroleum University, Chengdu 610500, China.

4 XJTU-Oxford Joint International Research Laboratory of Catalysis, School of Chemical Engineering and Technology, Xi'an Jiaotong University, Xi'an 710049, China.

* Corresponding author: Fan Dong (dongfan@uestc.edu.cn; dfctbu@126.com)

# Table of Context

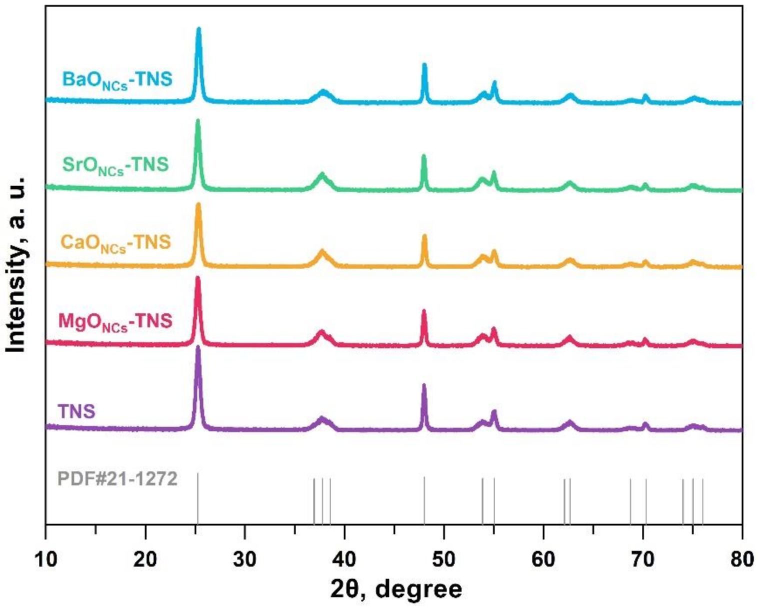

**Supplementary Figure 1.** XRD patterns for pristine and MO$_{NCs}$ deposited TNS.

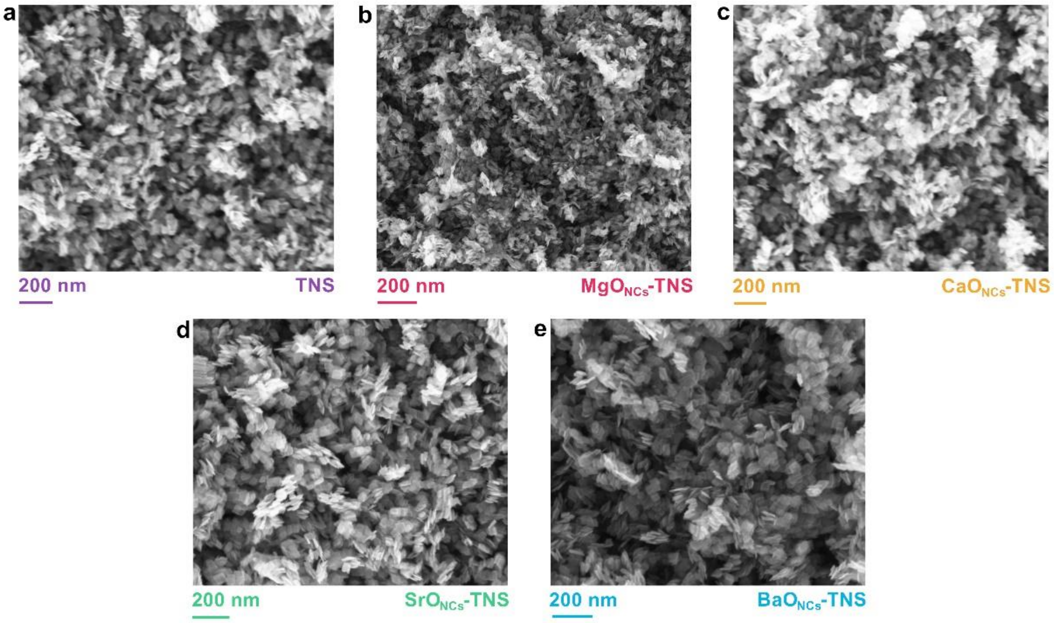

**Supplementary Figure 2.** SEM images TNS **(a)**, MgO$_{NCs}$-TNS **(b)**, CaO$_{NCs}$-TNS **(c)**, SrO$_{NCs}$-TNS **(d)** and BaO$_{NCs}$-TNS **(e)**.

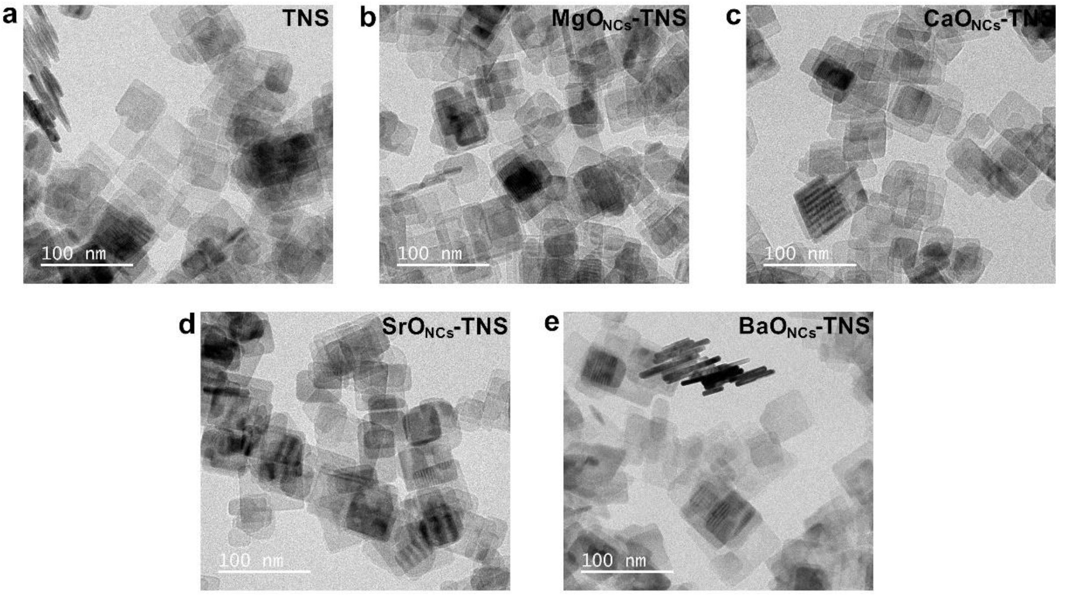

**Supplementary Figure 3.** TEM images of TNS **(a)**, MgO$_{\text{NCs}}$-TNS **(b)**, CaO$_{\text{NCs}}$-TNS **(c)**, SrO$_{\text{NCs}}$-TNS **(d)** and BaO$_{\text{NCs}}$-TNS **(e)**.

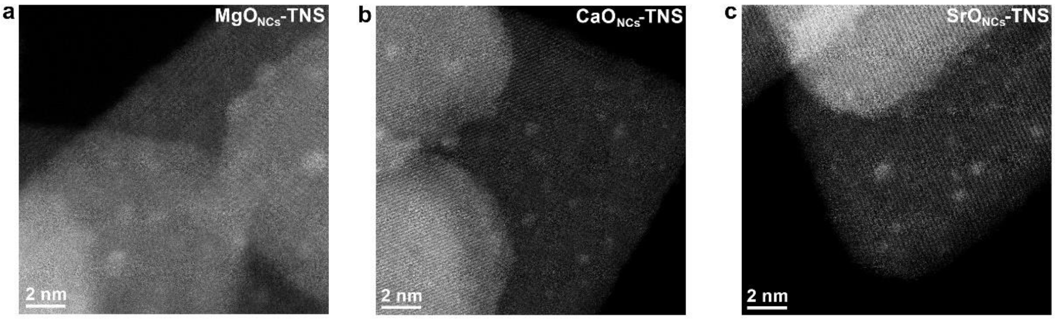

**Supplementary Figure 4.** HAADF-STEM for MgO$_{\text{NCs}}$-TNS **(a)**, CaO$_{\text{NCs}}$-TNS **(b)**, SrO$_{\text{NCs}}$-TNS **(c)**.

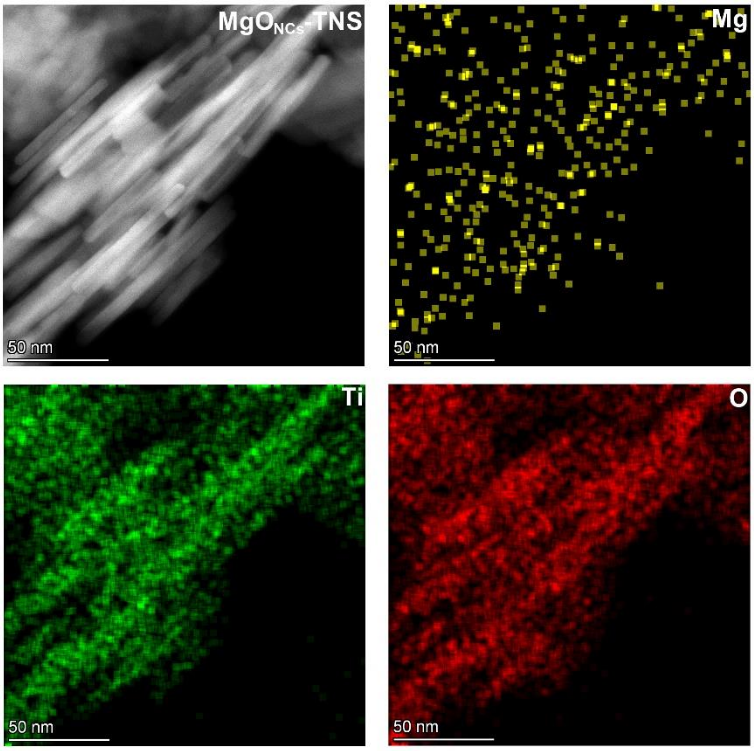

**Supplementary Figure 5.** TEM and elemental mapping images for MgO$_{NCs}$-TNS.

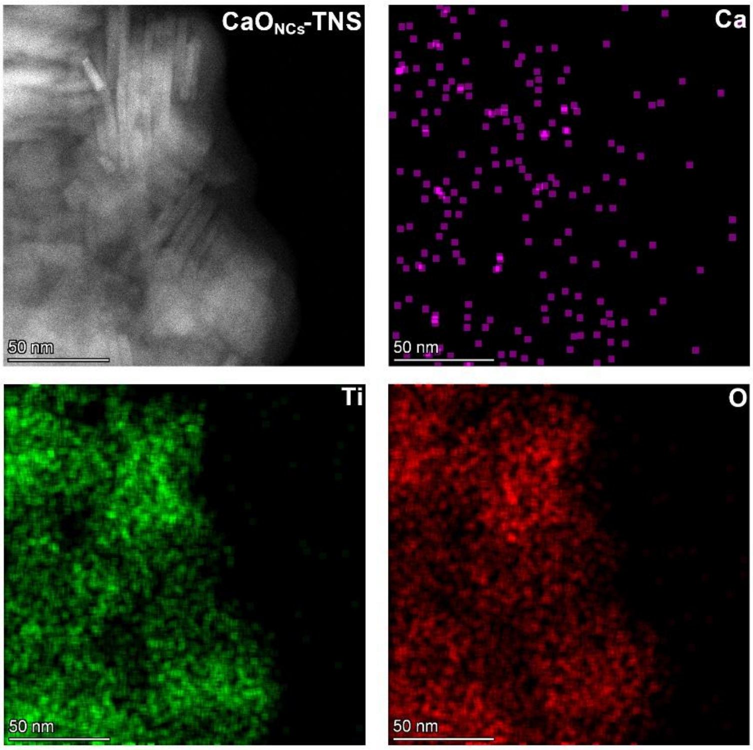

**Supplementary Figure 6.** TEM and elemental mapping images for CaO$_{NCs}$-TNS.

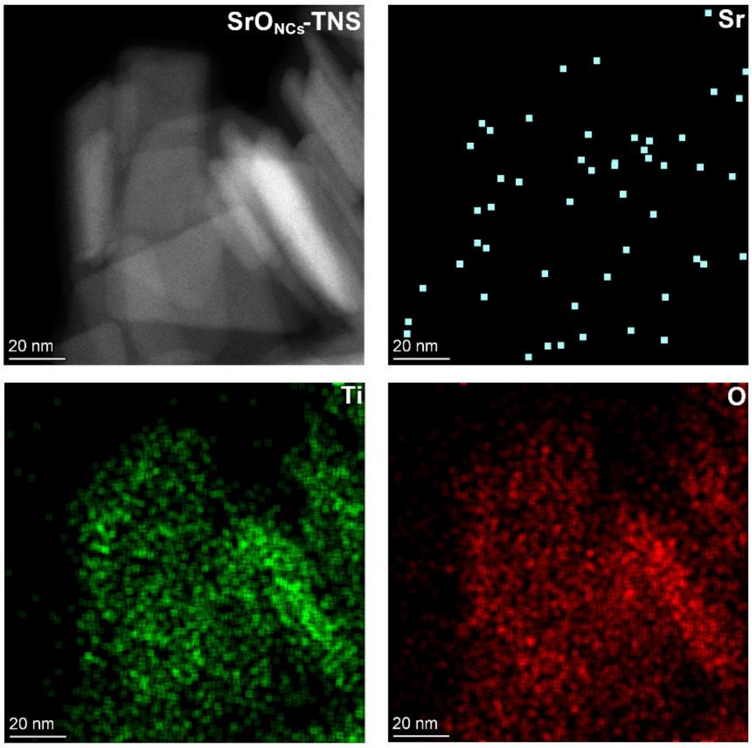

**Supplementary Figure 7.** TEM and elemental mapping images for $SrO_{NCs}$-TNS.

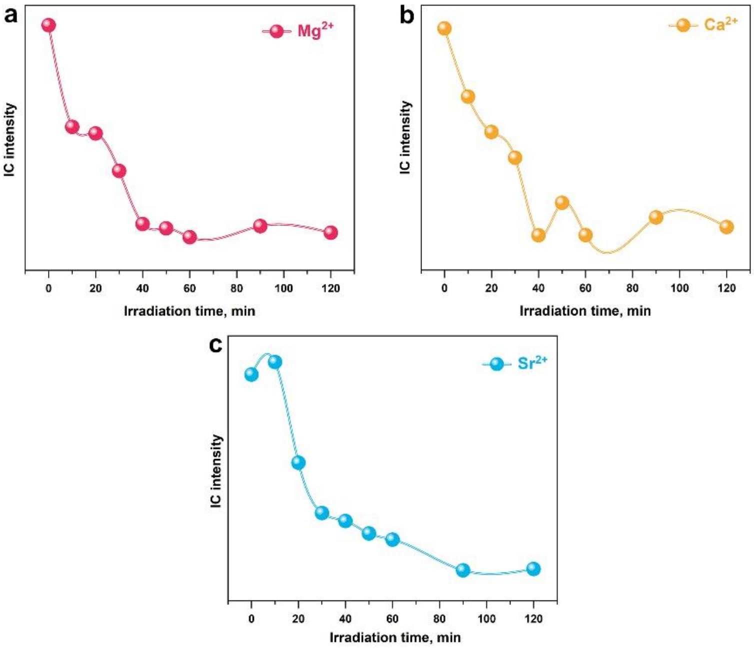

**Supplementary Figure 8.** Variation of IC signals for $Mg^{2+}$ **(a)**, $Ca^{2+}$ **(b)** and $Sr^{2+}$ **(c)** ions during the operando construction of corresponding $MO_{NCs}$ on TNS.

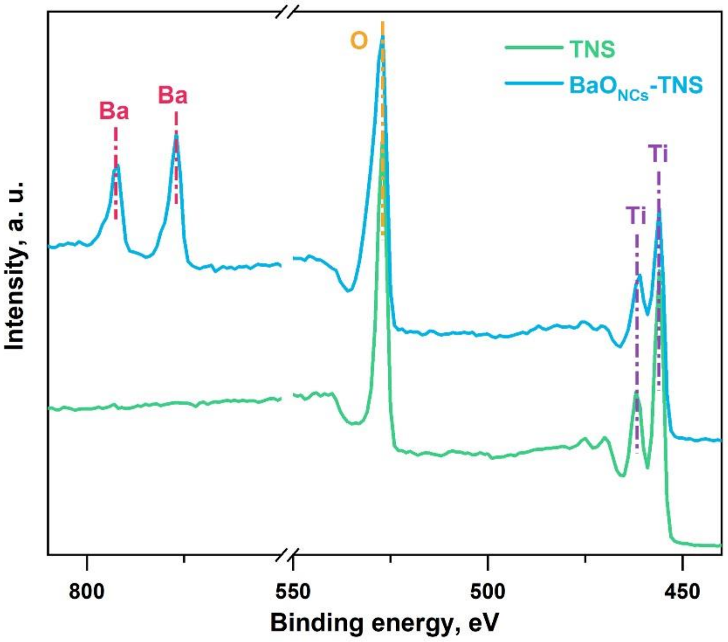

**Supplementary Figure 9.** XPS survey spectra for pristine and $BaO_{NCs}$ deposited TNS.

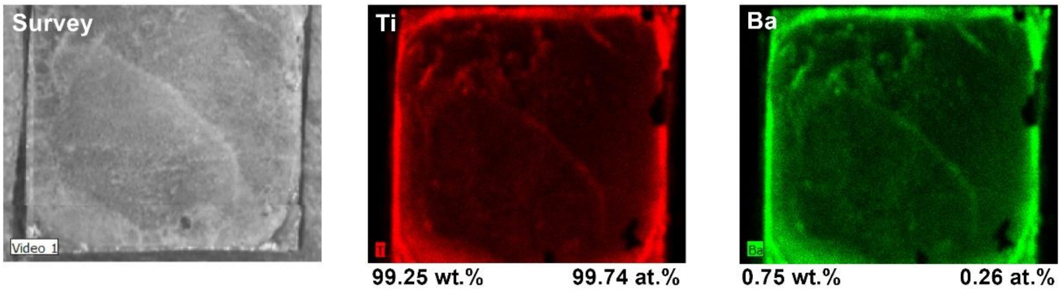

**Supplementary Figure 10.** XRF results for $BaO_{NCs}$-TNS.

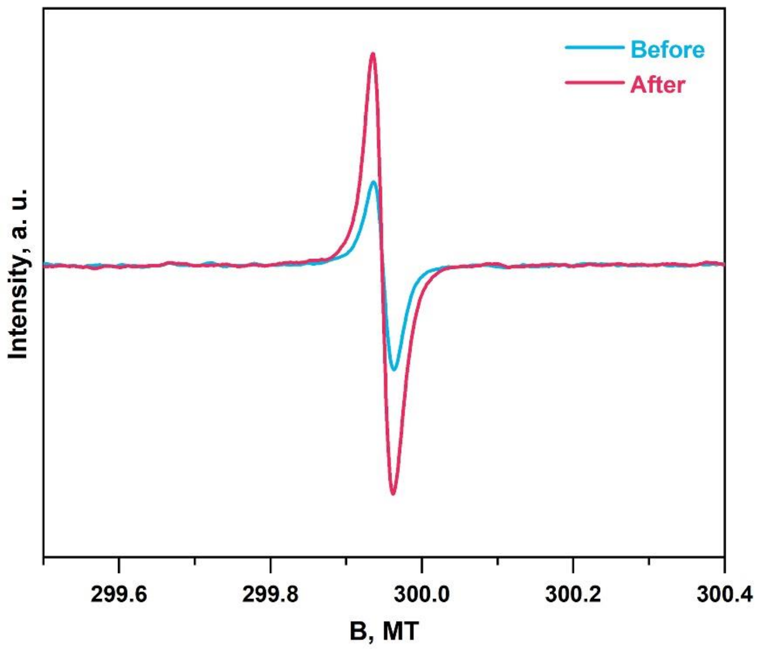

**Supplementary Figure 11.** Low temperature (120 K) solid-state EPR results of TNS before and after irradiation for 30 min.

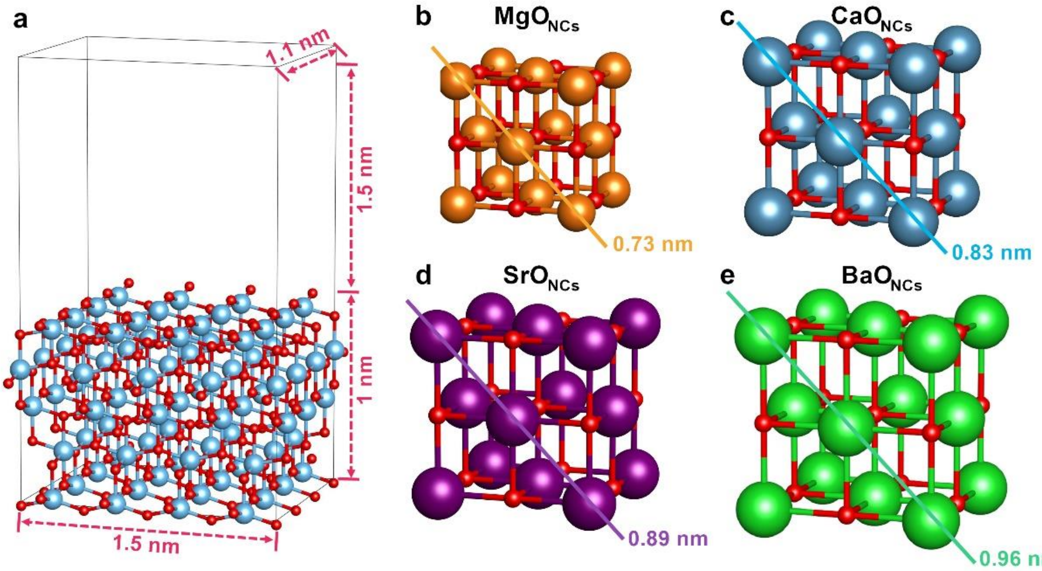

**Supplementary Figure 12.** Initial calculation models for pristine TNS **(a)**, $MgO_{NCs}$-TNS **(b)**, $CaO_{NCs}$-TNS **(c)**, $SrO_{NCs}$-TNS **(d)** and $BaO_{NCs}$-TNS **(e)**. The blue, red, orange, dark blue, purple and green spheres depict Ti, O, Mg, Ca, Sr and Ba atoms respectively.

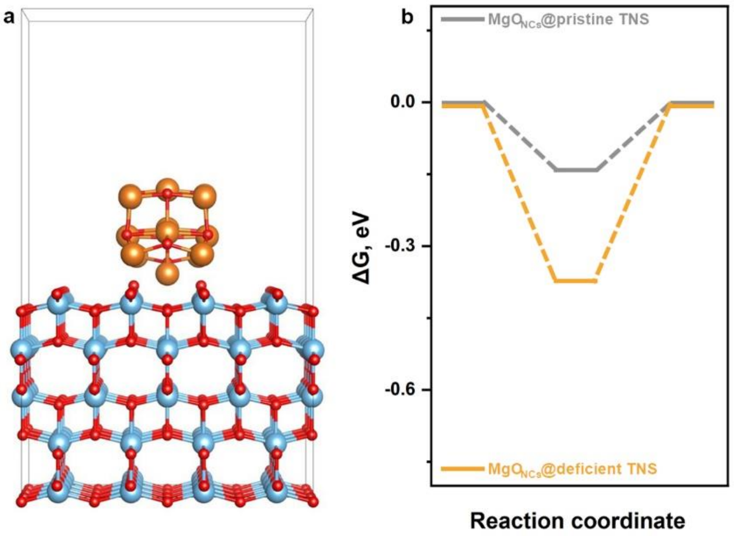

**Supplementary Figure 13. a.** Relaxed micro-structure of $MgO_{NCs}$ deposited at TNS surface. The blue, red and orange spheres depict Ti, O and Mg atoms respectively. **b.** Calculated binding energy of $BaO_{NCs}$ deposited at pristine and deficient TNS surfaces, respectively.

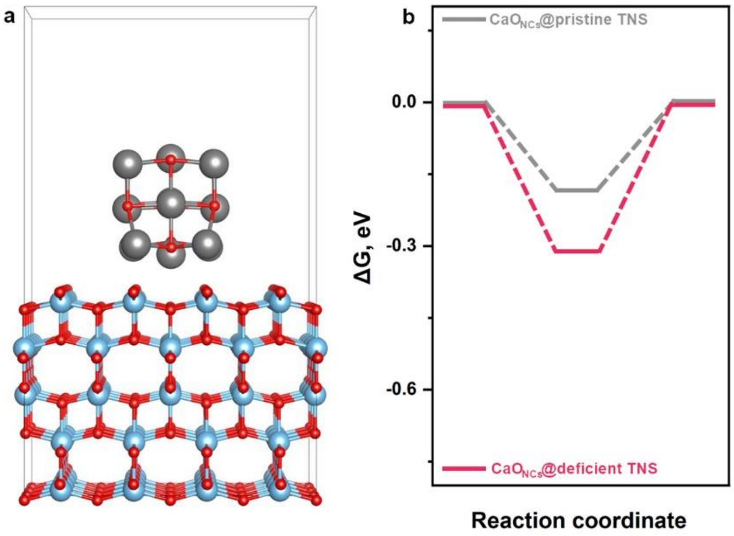

**Supplementary Figure 14. a.** Relaxed micro-structure of CaO$_{NCs}$ deposited at TNS surface. The blue, red and grey spheres depict Ti, O and Ca atoms respectively. **b.** Calculated binding energy of CaO$_{NCs}$ deposited at pristine and deficient TNS surfaces respectively.

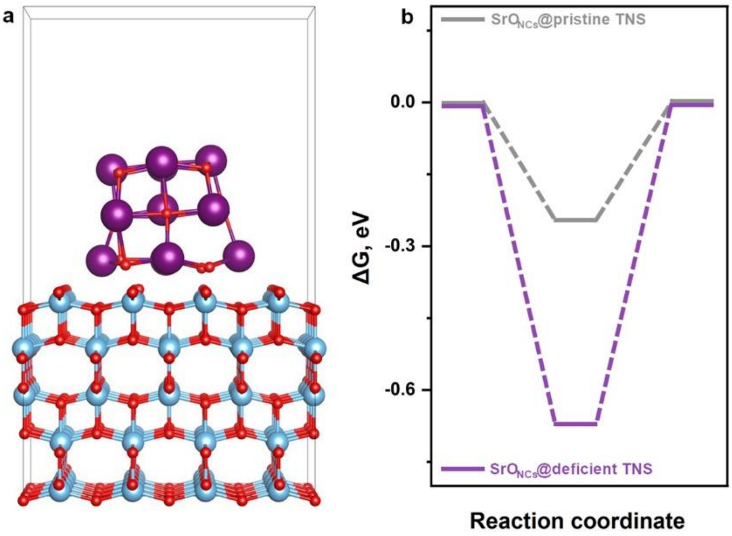

**Supplementary Figure 15. a.** Relaxed micro-structure of SrO$_{NCs}$ deposited at TNS surface. The blue, red and purple spheres depict Ti, O and Sr atoms respectively. **b.** Calculated binding energy of SrO$_{NCs}$ deposited at pristine and deficient TNS surfaces respectively.

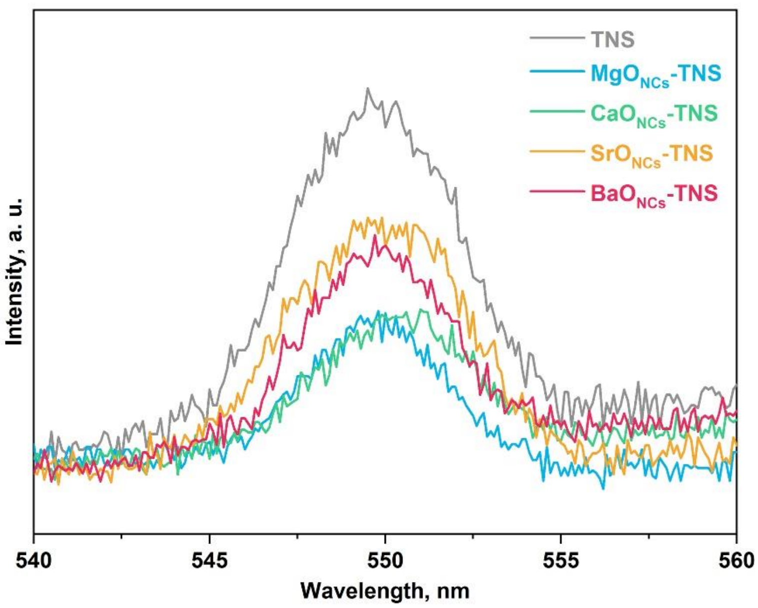

**Supplementary Figure 16.** PL spectra for pristine TNS, $MgO_{NCs}$-TNS, $CaO_{NCs}$-TNS, $SrO_{NCs}$-TNS and $BaO_{NCs}$-TNS, respectively.

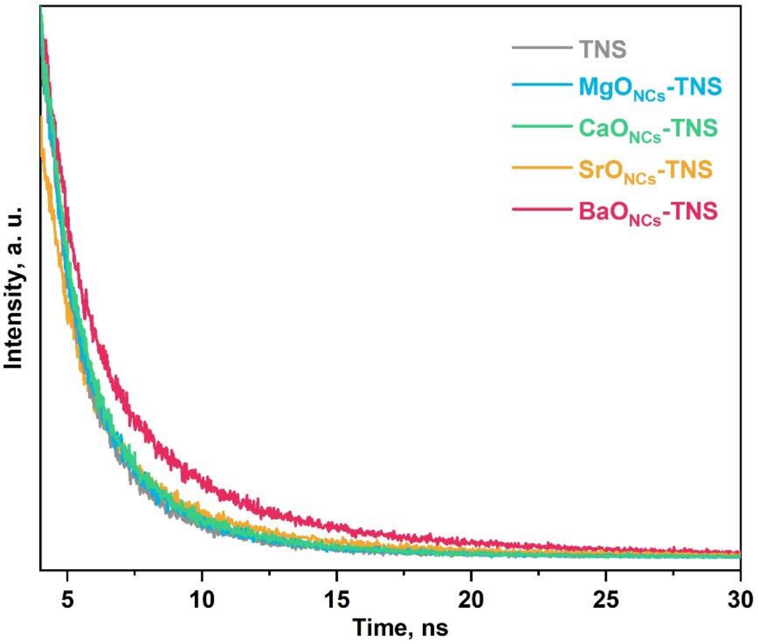

**Supplementary Figure 17.** Time-resolved fluorescence emission decay spectra for pristine TNS, $MgO_{NCs}$-TNS, $CaO_{NCs}$-TNS, $SrO_{NCs}$-TNS and $BaO_{NCs}$-TNS, respectively.

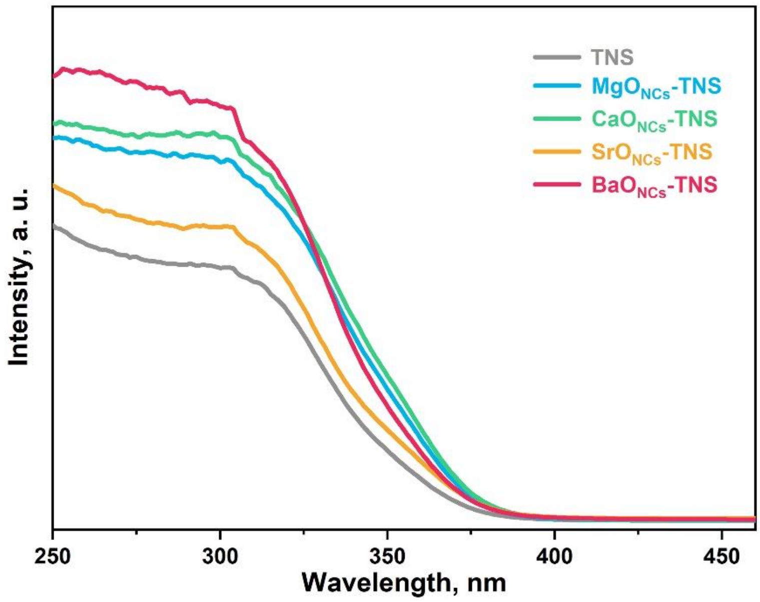

**Supplementary Figure 18.** UV-vis DRS results for pristine TNS, $MgO_{NCs}$-TNS, $CaO_{NCs}$-TNS, $SrO_{NCs}$-TNS and $BaO_{NCs}$-TNS, respectively.

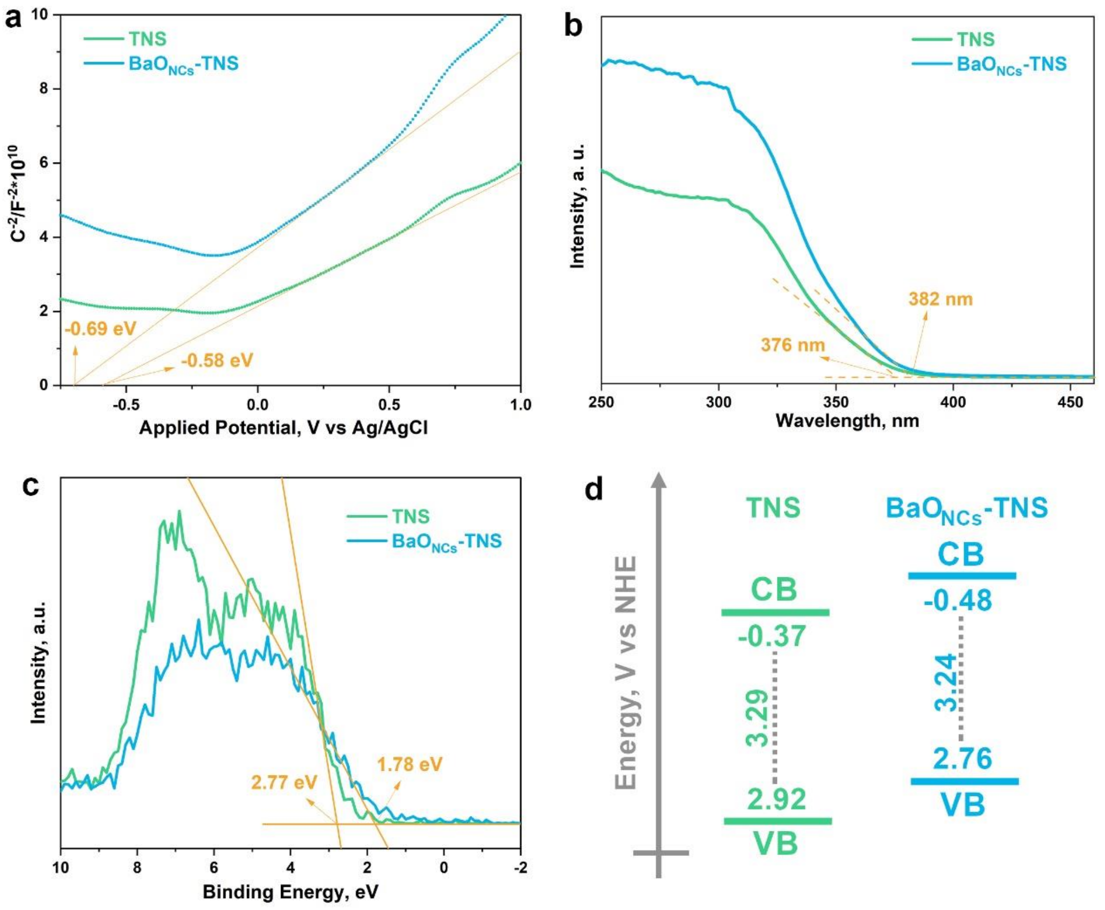

**Supplementary Figure 19.** Estimated band structures. Mott-Schottky spectra (a), estimated band gap calculated by UV-vis DRS (b), XPS VB spectra (c) and illustration for the band structures of TNS and BaO$_{NCs}$-TNS.

Since the contaminative C element is inevitable during the XPS tests, the band edge cannot be precisely characterized by the XPS VB spectra. Hence the Mott-Schottky spectra and UV-vis DRS were combined to determine the band structures of TNS and BaO$_{NCs}$-TNS.

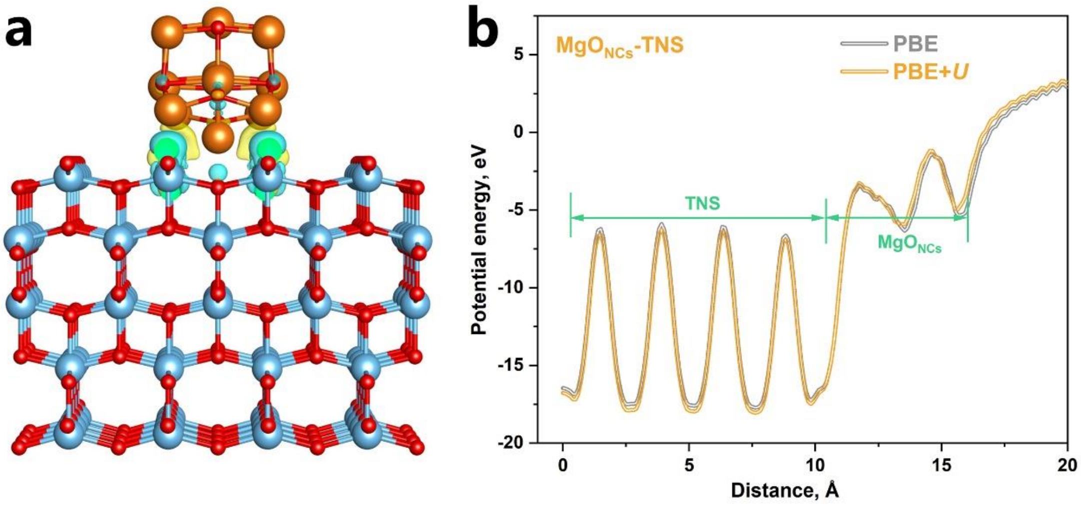

**Supplementary Figure 20.** Calculated charge difference density **(a)** and planer average potential energy profile **(b)** for the interface between MgO$_{NCs}$ and TNS. The charge accumulation is labeled in blue and charge depletion is labeled in yellow. The isosurface was set to 0.0047 eV Å$^{-3}$. Blue, red and orange spheres depict Ti, O and Mg atoms, respectively.

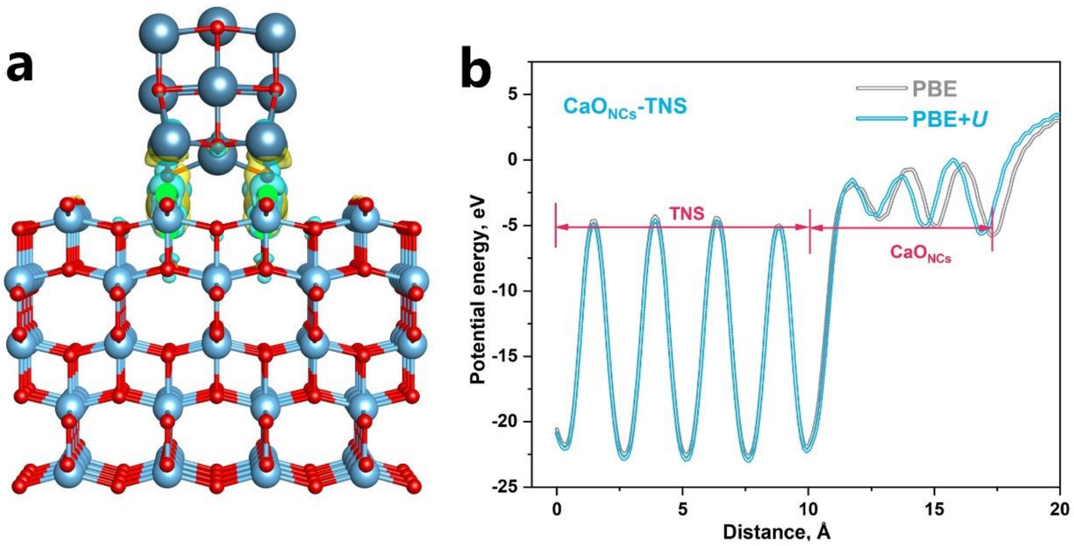

**Supplementary Figure 21.** Calculated charge difference density **(a)** and planer average potential energy profile **(b)** for the interface between CaO$_{NCs}$ and TNS. The charge accumulation is labeled in blue and charge depletion is labeled in yellow. The isosurface was set to 0.005 eV Å$^{-3}$. Blue, red and cyan spheres depict Ti, O and Ca atoms, respectively.

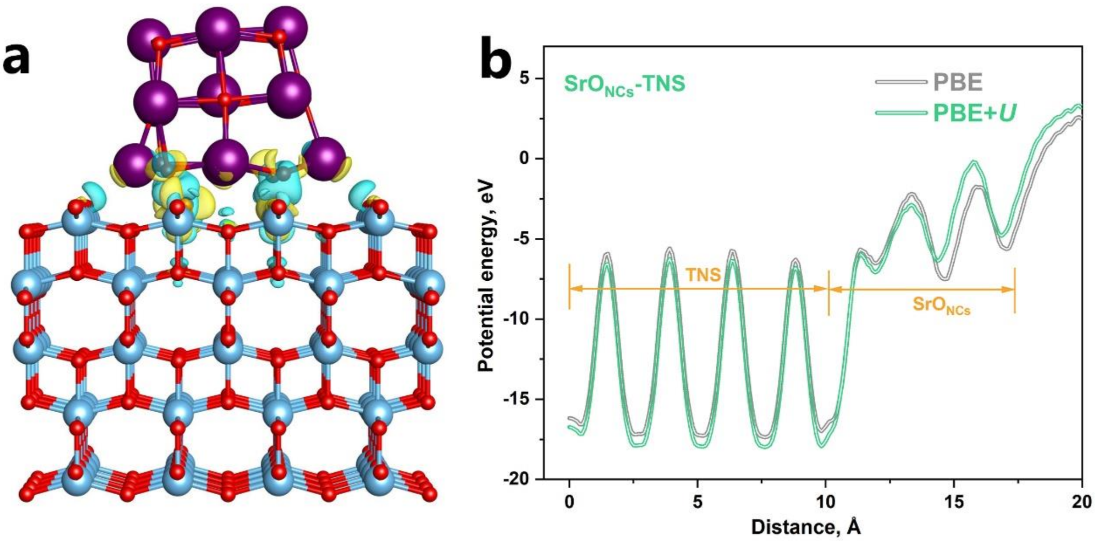

**Supplementary Figure 22.** Calculated charge difference density **(a)** and planer average potential energy profile **(b)** for the interface between SrO$_{NCs}$ and TNS. The charge accumulation is labeled in blue and charge depletion is labeled in yellow. The isosurface was set to 0.005 eV Å$^{-3}$. Blue, red and purple spheres depict Ti, O and Sr atoms respectively.

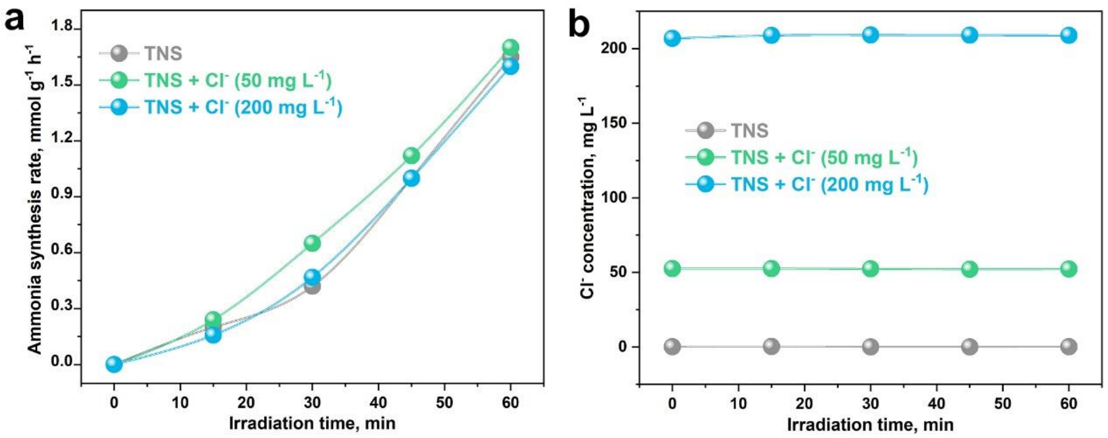

**Supplementary Figure 23.** Controlled experiment by adding Cl$^-$ into the catalysis system of pristine without other cations or anions.

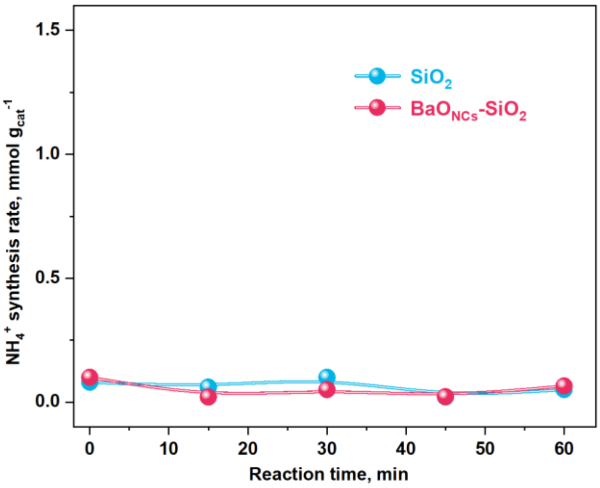

**Supplementary Figure 24.** Control experiment towards NO$_3^-$RR to NH$_4^+$ synthesis by replacing TiO$_2$ with SiO$_2$. The test parameters were the same with that of Fig. 3a.

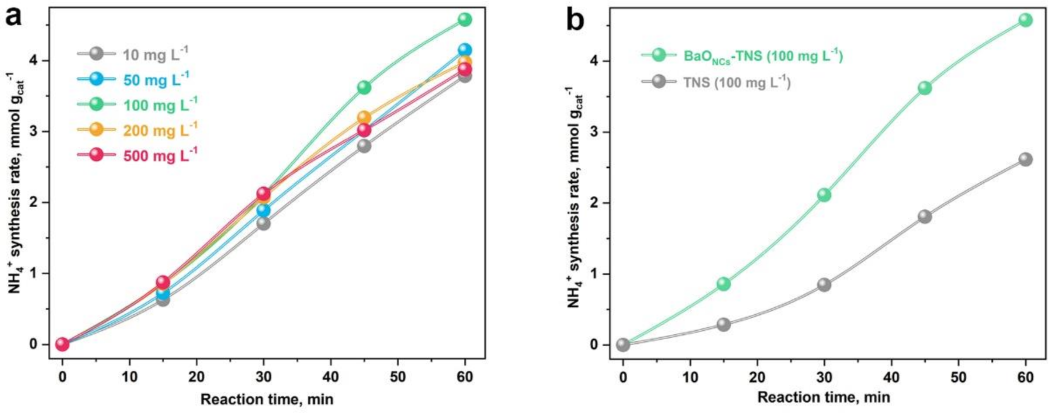

**Supplementary Figure 25.** Initial $NO_3^-$ concentration optimization on $BaO_{NCs}$-TNS for the promotion of $NH_4^+$ photosynthesis efficiency **(a)** and its comparison towards the pristine TNS **(b)**.

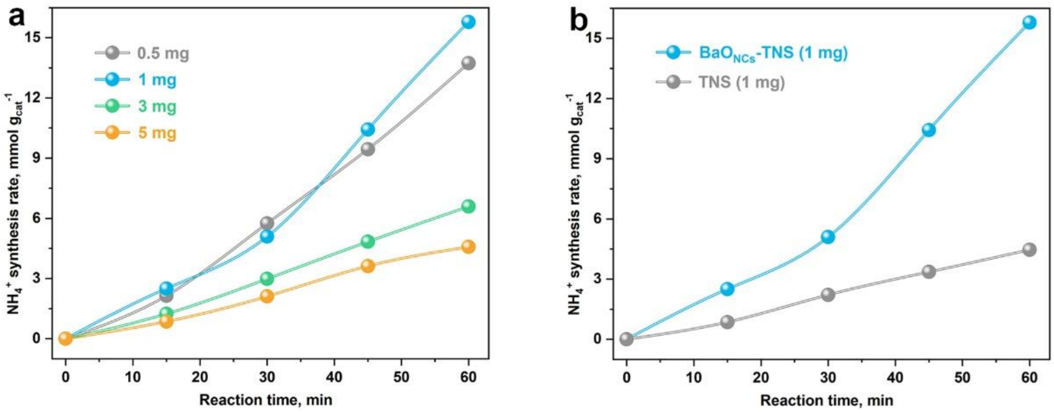

**Supplementary Figure 26.** Catalyst dosage optimization on $BaO_{NCs}$-TNS for the promotion of $NH_4^+$ photosynthesis efficiency **(a)** and its comparison towards the pristine TNS **(b)**.

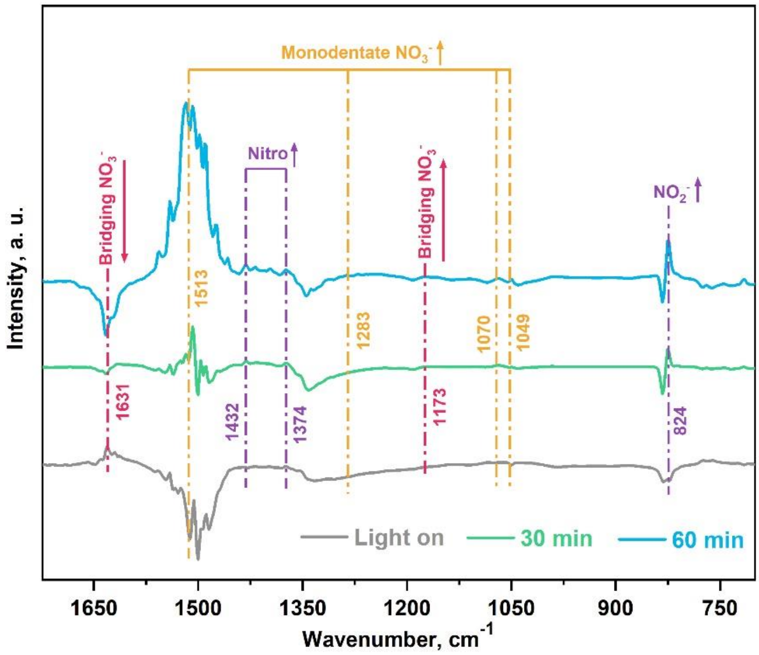

**Supplementary Figure 27.** *In-situ* DRIFTS results for the preactivation of $NO_3^-$ by UV light irradiation.

The test procedure is similar with that of the in-situ DRIFTS test in Fig. 5b by replacing the $NO_3^-$-contained catalyst with pristine $KNO_3$ powder. It is observed in the above figure that some bridging $NO_3^-$ (1631 and 1173 $cm^{-1}$)[1, 2] is transferred into the monodentate $NO_3^-$ species (1513, 1283, 1070 and 1049 $cm^{-1}$)[2, 3], which is more active than that of the bridging $NO_3^-$ [4]. Moreover, the intermediated nitro (-$NO_2$, 1432 and 1374 $cm^{-1}$)[4] and $NO_2^-$ (824 $cm^{-1}$) are obviously increased. It is concluded that the $NO_3^-$ reactant can be preactivated by UV light irradiation.

**Supplementary reference:**

1 Zhang, X. L., He, H, Cao, H. W. & Yu, Y. B. Experimental and theoretical studies of surface nitrate species on Ag/$Al_2O_3$ using DRIFTS and DFT. *Spectrochim. Acta A*, **71**, 1446-1451 (2008).

2 Yang, X. F. *et al.* DRIFTS Study of Ammonia Activation over CaO and Sulfated CaO for NO Reduction by $NH_3$. *Environ. Sci. Technol.*, **45**, 1147-1151 (2011).

3 Cui, W. *et al.* Highly Efficient Performance and Conversion Pathway of Photocatalytic NO Oxidation on SrO-Clusters@Amorphous Carbon Nitride. *Environ. Sci. Technol.*, **51**, 10682-10690 (2017).

4 Hadjiivanov, K. Identification of Neutral and Charged $N_xO_y$ Surface Species by IR

Spectroscopy. *Catal. Rev. Sci. Eng.*, **42**, 71-144 (2000).

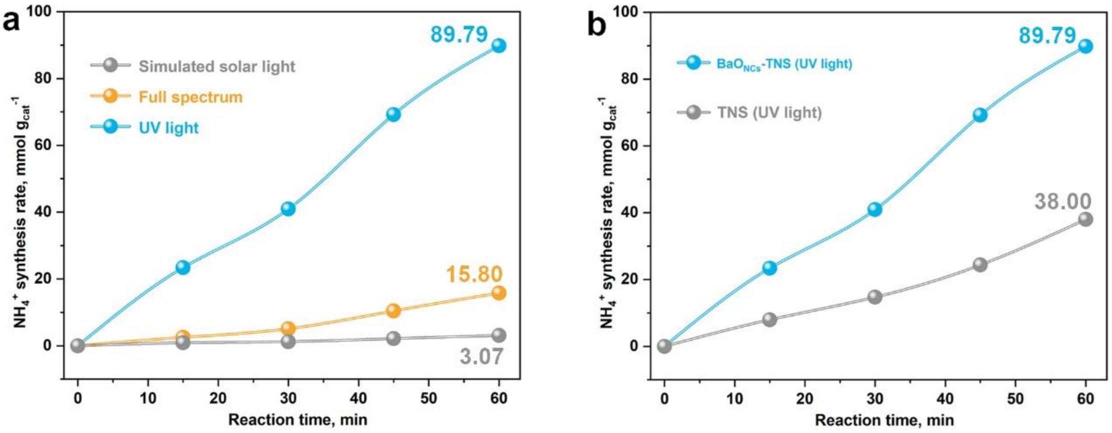

**Supplementary Figure 28.** Light source optimization on BaO$_{NCs}$-TNS for the promotion of NH$_4^+$ photosynthesis efficiency **(a)** and its comparison towards the pristine TNS **(b)**.

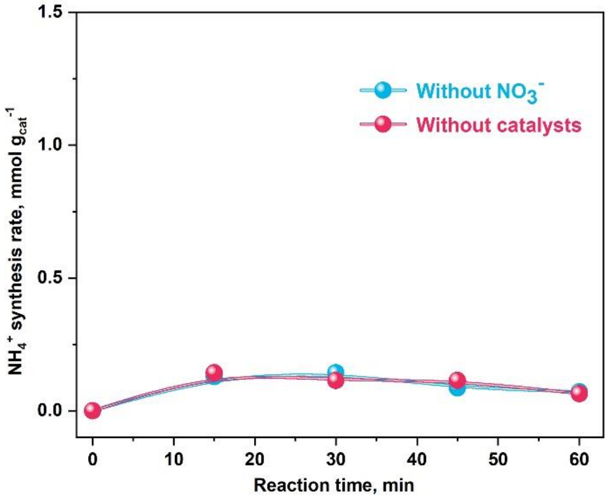

**Supplementary Figure 29.** Blank control experiment excluding the contribution of contaminative N source to $NH_4^+$ photosynthesis by conducting the photocatalytic activity evaluation without $NO_3^-$ and catalysts respectively.

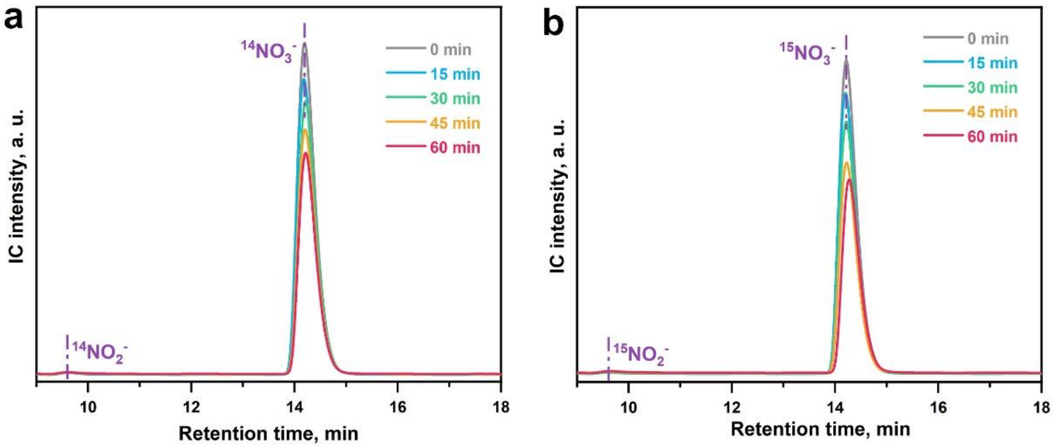

**Supplementary Figure 30.** Detected IC signals for $^{14}NO_3^-$/$^{14}NO_2^-$ **(a)** and $^{15}NO_3^-$/$^{15}NO_2^-$ **(b)** during the reaction process. The ranges of y axis were set consistently for both **(a)** and **(b)**.

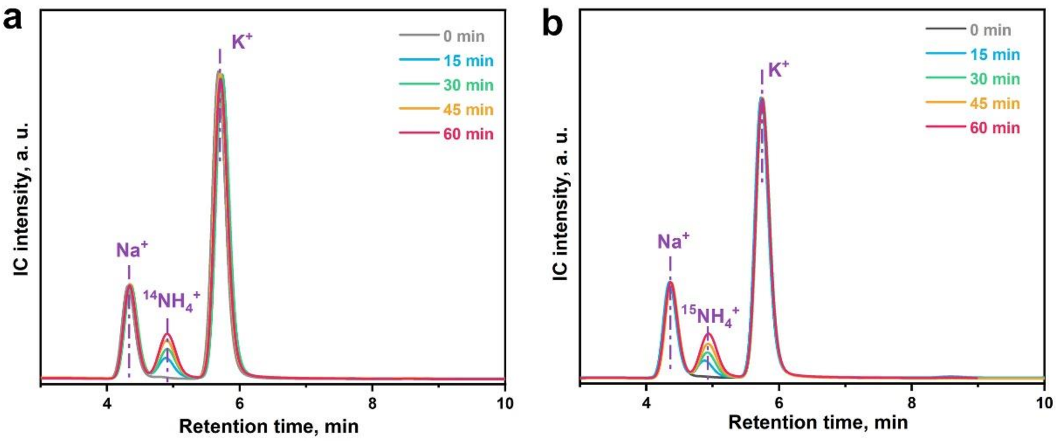

**Supplementary Figure 31.** Detected IC signals for $^{14}NH_4^+$ **(a)** and $^{15}NH_4^+$ **(b)** during the reaction process. The ranges of y axis were set consistently for both **(a)** and **(b)**.

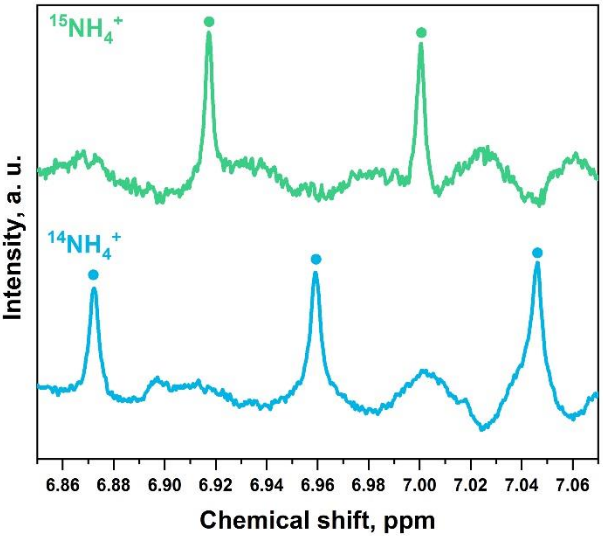

**Supplementary Figure 32.** $^1H$ NMR spectra of the produced $NH_4^+$ using $^{14}NO_3^-$ and $^{15}NO_3^-$ as the nitrogen source respectively.

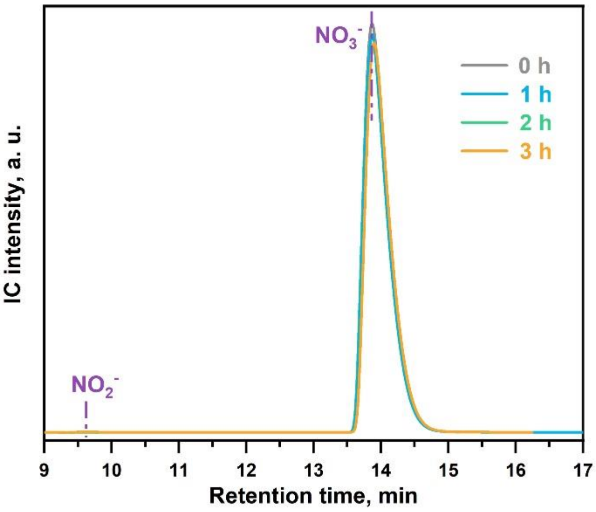

**Supplementary Figure 33.** Detected IC signals for $NO_3^-$ consumption and $NO_2^-$ generation in the selectivity tests.

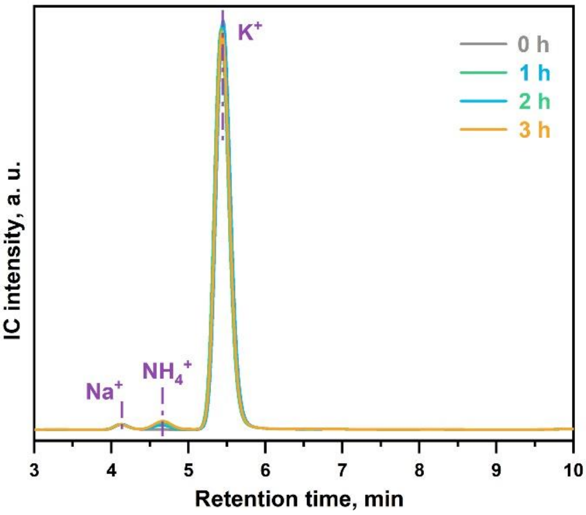

**Supplementary Figure 34.** Detected IC signals for $NH_4^+$ generation in the selectivity tests.

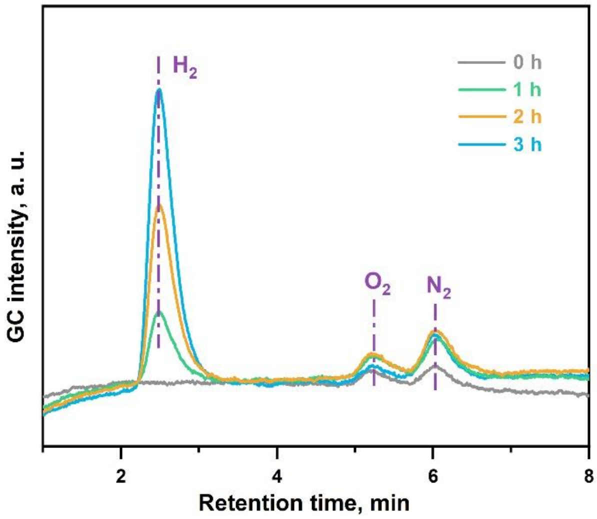

**Supplementary Figure 35.** Detected GC signals for $H_2$ generation in the selectivity tests.

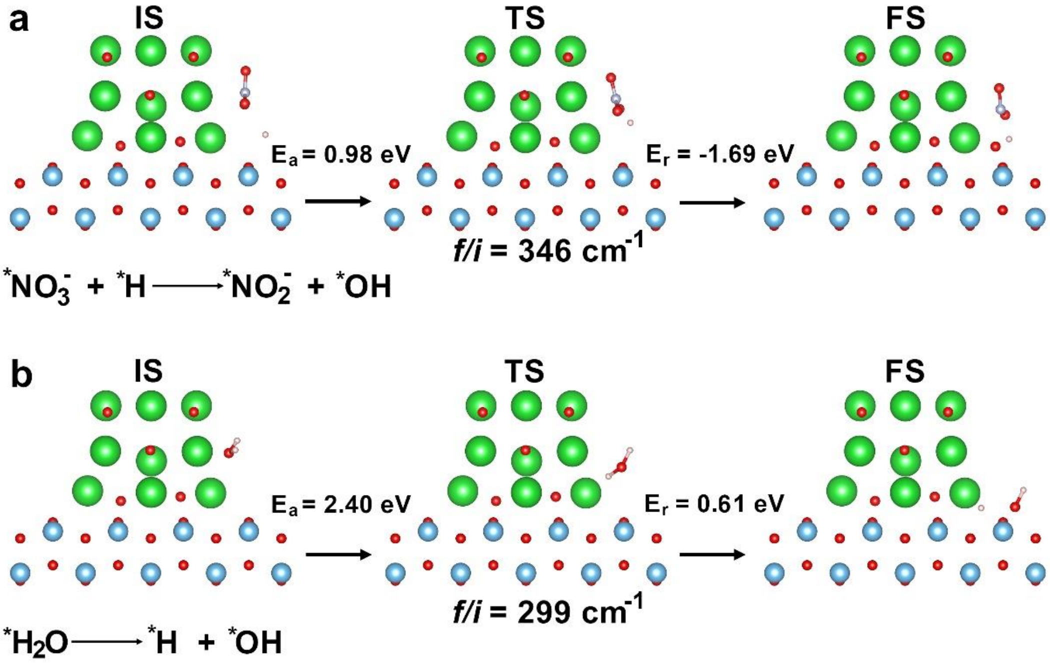

**Supplementary Figure 36.** Calculated reaction coordinates of $NO_3^-$ reduction **(a)** and water splitting **(b)**. The transition state was identified when a single imaginary frequency was located and all forces on atoms were zero. The blue, red, green, light grey and pink spheres depict Ti, O, Ba, N and H atoms, respectively.

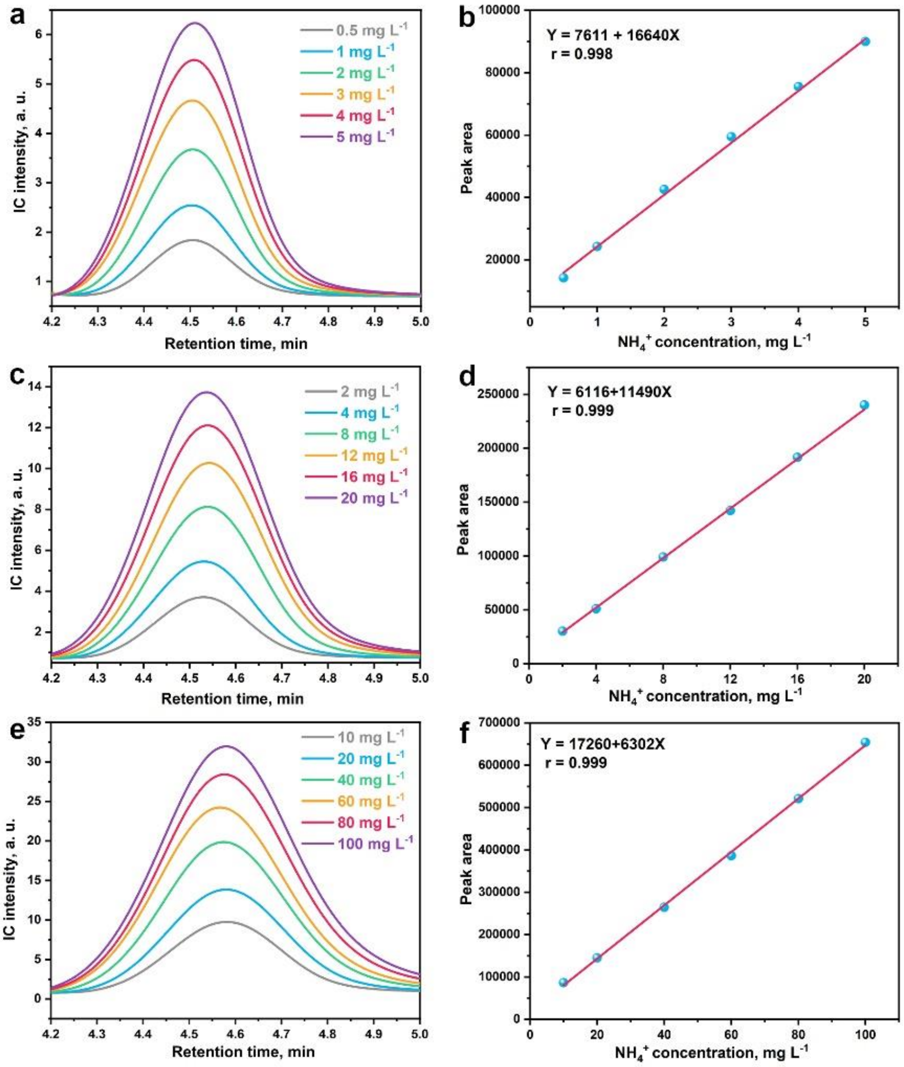

**Supplementary Figure 37.** Plotting of standard curves of NH$_4^+$ in the concentration range of 0.5-5 mg L$^{-1}$ (**a and b**), 2-20 mg L$^{-1}$ (**c and d**) and 10-100 mg L$^{-1}$ (**e and f**) respectively by IC detection.

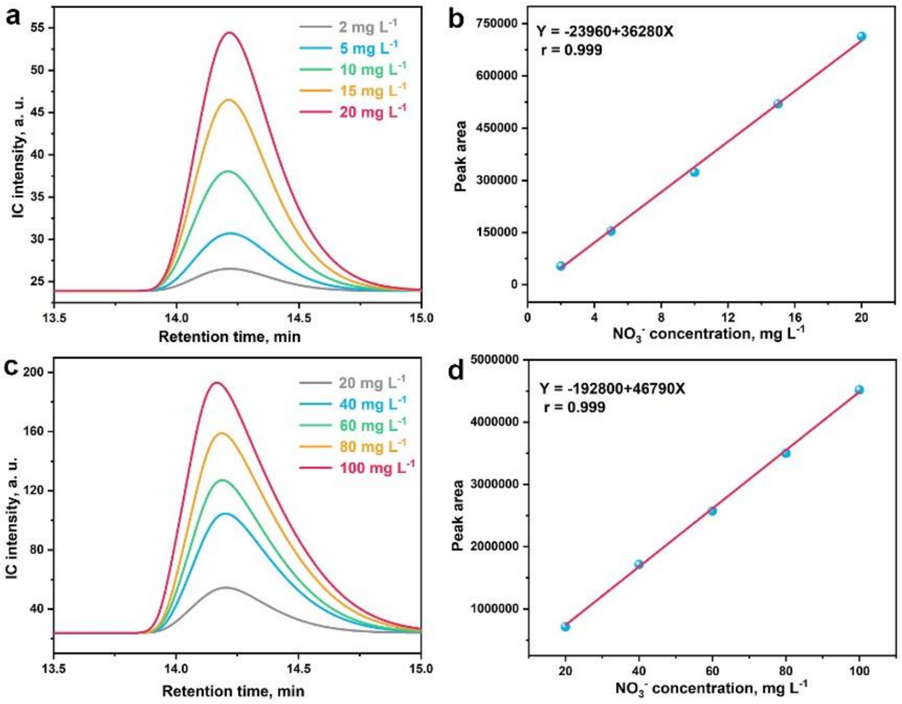

**Supplementary Figure 38.** Plotting of standard curves of $NO_3^-$ in the concentration range of 2-20 mg L$^{-1}$ (**a and b**) and 20-100 mg L$^{-1}$ (**c and d**) respectively by IC detection.

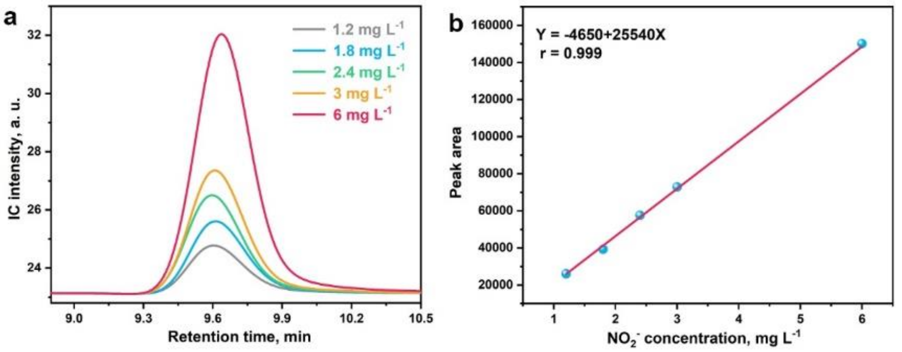

**Supplementary Figure 39.** Plotting of standard curves of $NO_2^-$ in the concentration range of 1.2-6 mg L$^{-1}$ by IC detection.

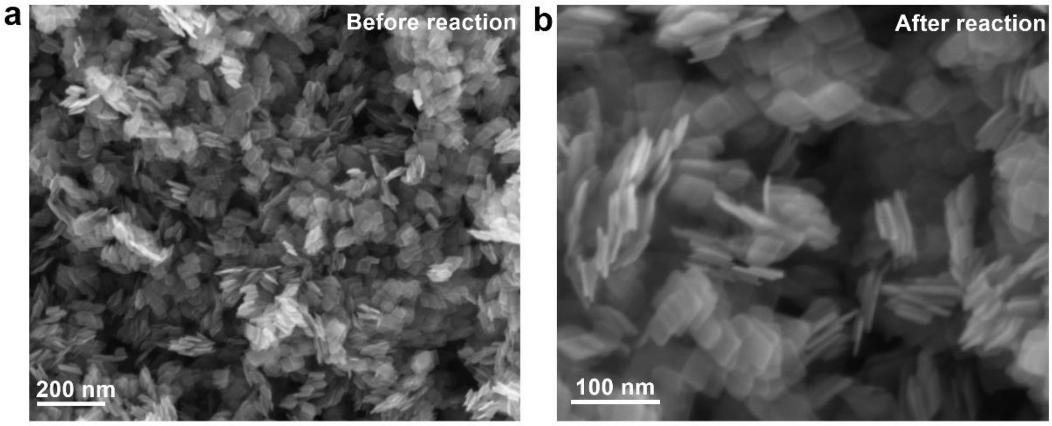

**Supplementary Figure 40.** SEM images for BaO$_{\text{NCs}}$-TNS before **(a)** and after **(b)** the $NH_4^+$ photosynthesis reaction.

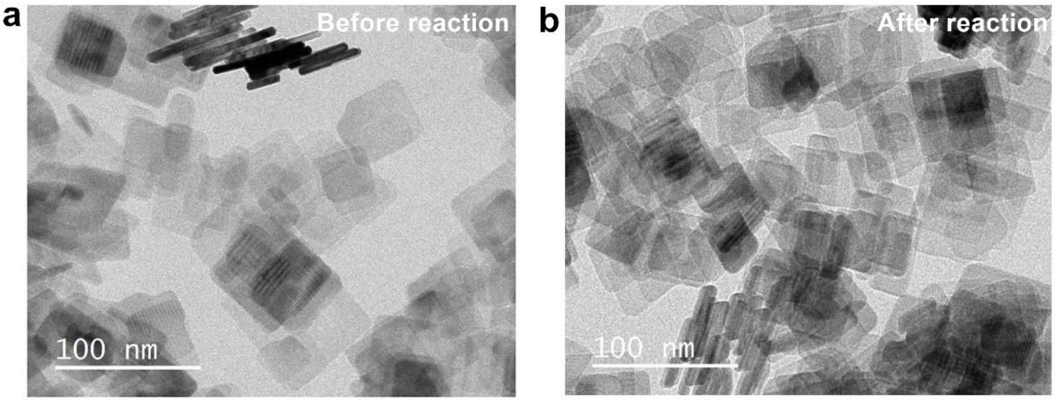

**Supplementary Figure 41.** TEM images for BaO$_{\text{NCs}}$-TNS before **(a)** and after **(b)** the $NH_4^+$ photosynthesis reaction.

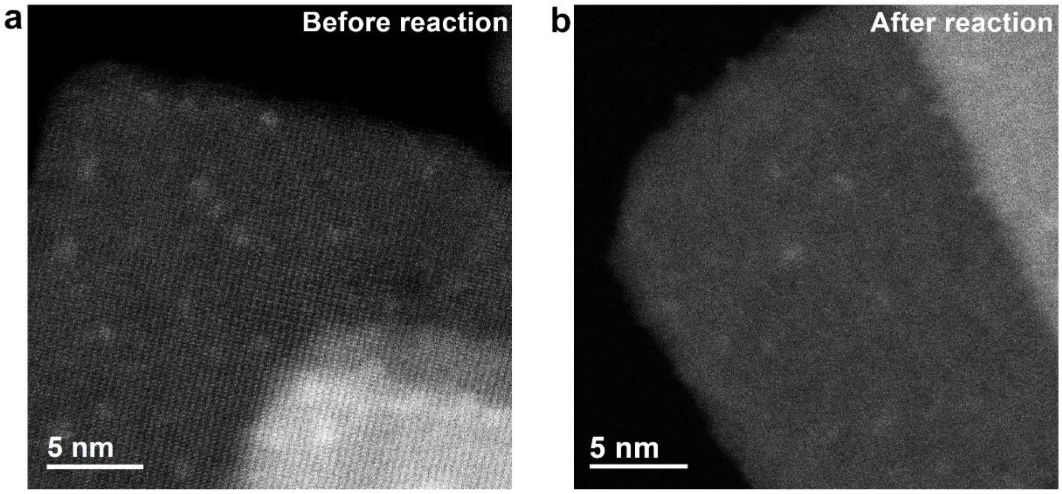

**Supplementary Figure 42.** HAADF-STEM images for BaO$_{\text{NCs}}$-TNS before **(a)** and after **(b)** the $NH_4^+$ photosynthesis reaction.

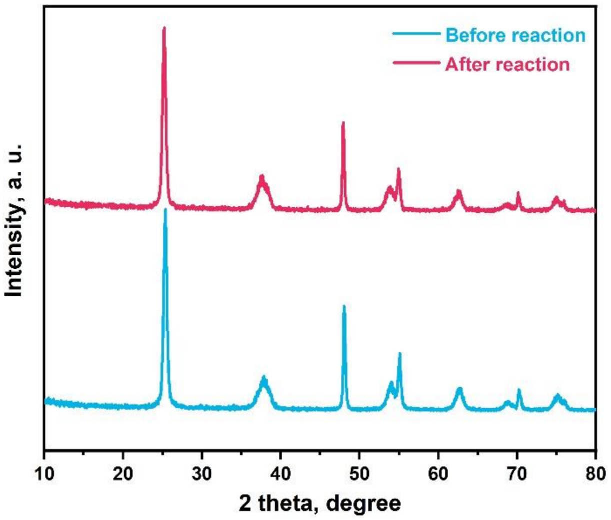

**Supplementary Figure 43.** XRD patterns for BaO$_{\text{NCs}}$-TNS before and after the $NH_4^+$ photosynthesis reaction.

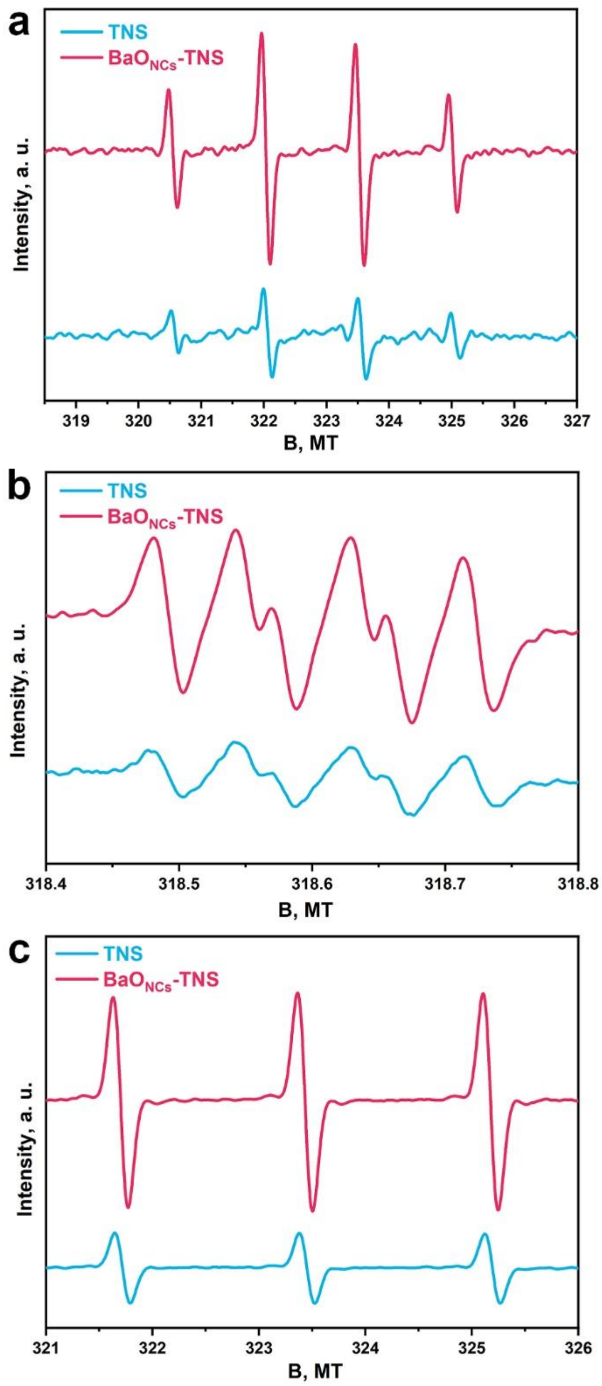

**Supplementary Figure 44.** Liquid-state EPR results for the detection of light-generated $^{\bullet}OH$ (**a**), $^{\bullet}O_2^-$ (**b**) and $^1O_2$ (**c**) radicals on the pristine and BaO$_{NCs}$ deposited TNS.

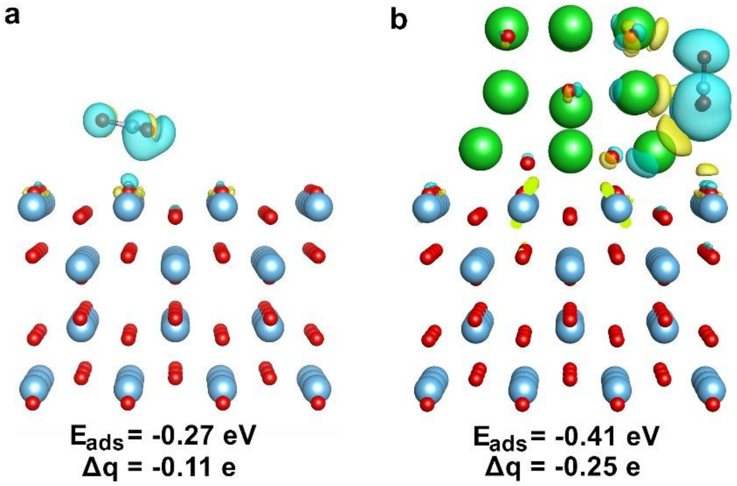

**Supplementary Figure 45.** Calculated results for $NO_3^-$ adsorption at the pristine (a) and $BaO_{NCs}$ deposited (b) TNS respectively. The blue, red, green and light grey spheres depict Ti, O, Ba and N atoms, respectively. The charge accumulation is labeled in blue and charge depletion is labeled in yellow. The isosurface was set to 0.015 eV Å$^{-3}$.

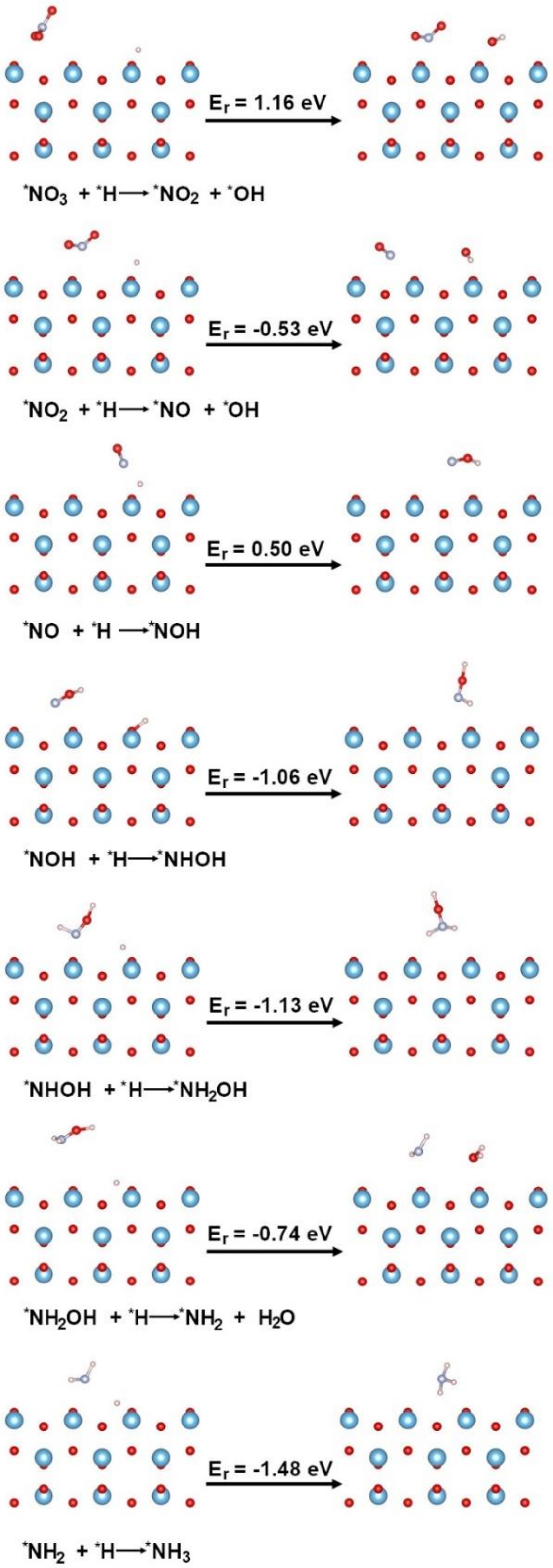

**Supplementary Figure 46.** Calculated reaction coordinates for $NO_3^-$ reduction at the pristine TNS surface (corresponding to the green line in Fig. 5c). The blue, red, light grey and pink spheres depict Ti, O, N and H atoms, respectively.

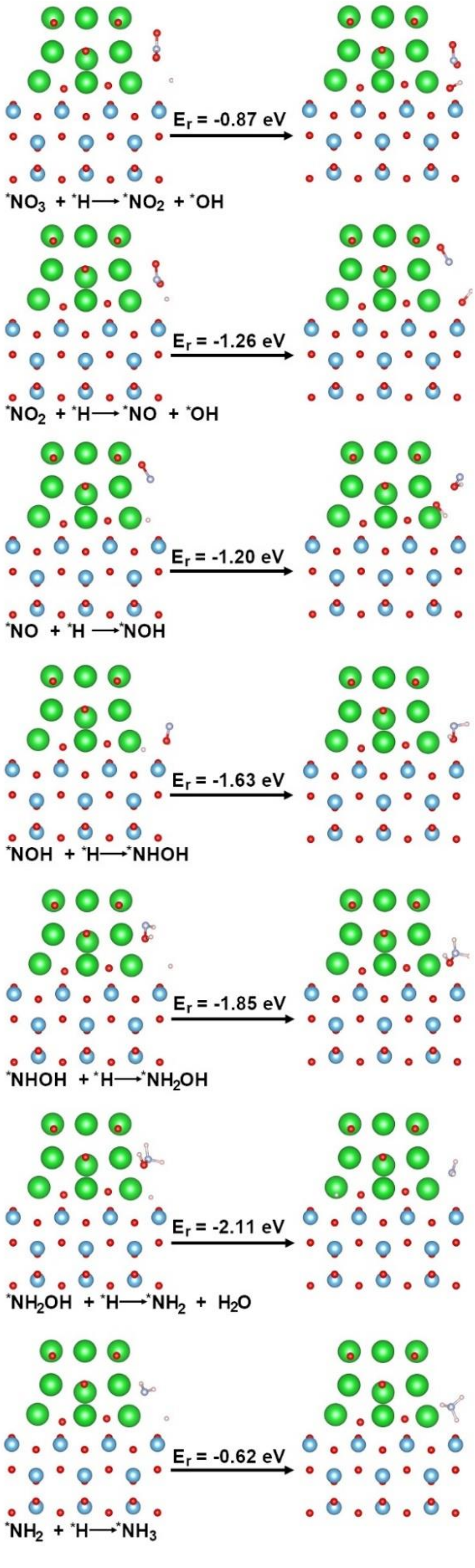

**Supplementary Figure 47.** Calculated reaction coordinates for $NO_3^-$ reduction at the $BaO_{NCs}$-TNS surface (corresponding to the blue line in Fig. 5c). The blue, red, green, light grey and pink spheres depict Ti, O, Ba, N and H atoms, respectively.

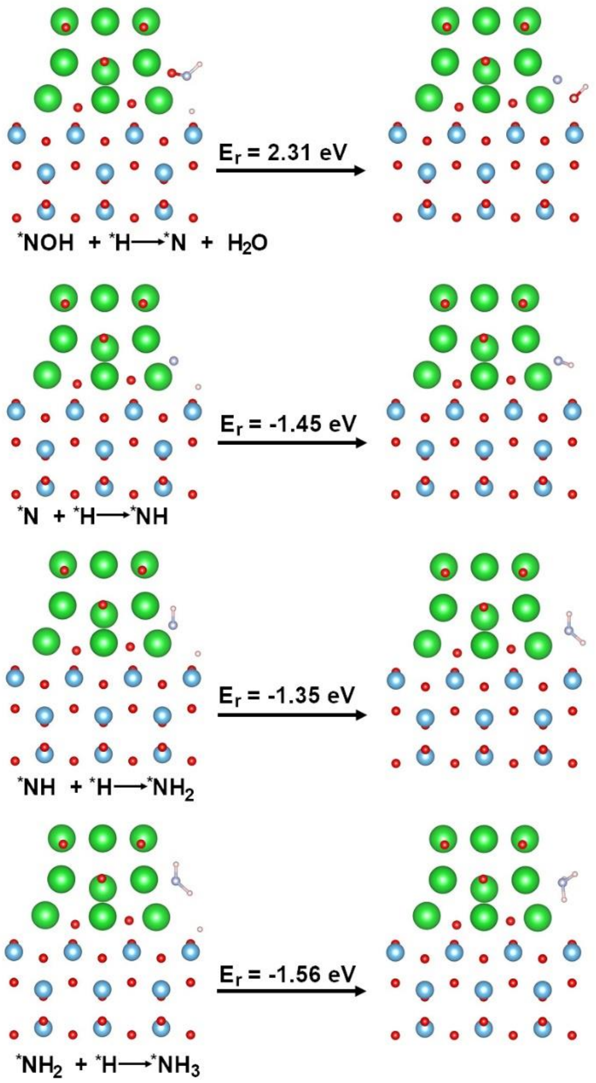

**Supplementary Figure 48.** Calculated reaction coordinates for the potential side reactions at the $BaO_{NCs}$-TNS surface (corresponding to the red line in Fig. 5c). The blue, red, green, light grey and pink spheres depict Ti, O, Ba, N and H, atoms respectively.

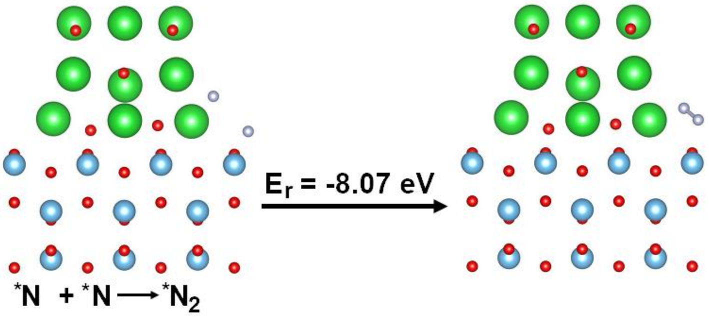

**Supplementary Figure 49.** Calculated reaction coordinates for the potential side reactions at the $BaO_{NCs}$-TNS surface (corresponding to the purple line in Fig. 5c). The blue, red, green, light grey and pink spheres depict Ti, O, Ba, N and H atoms, respectively.

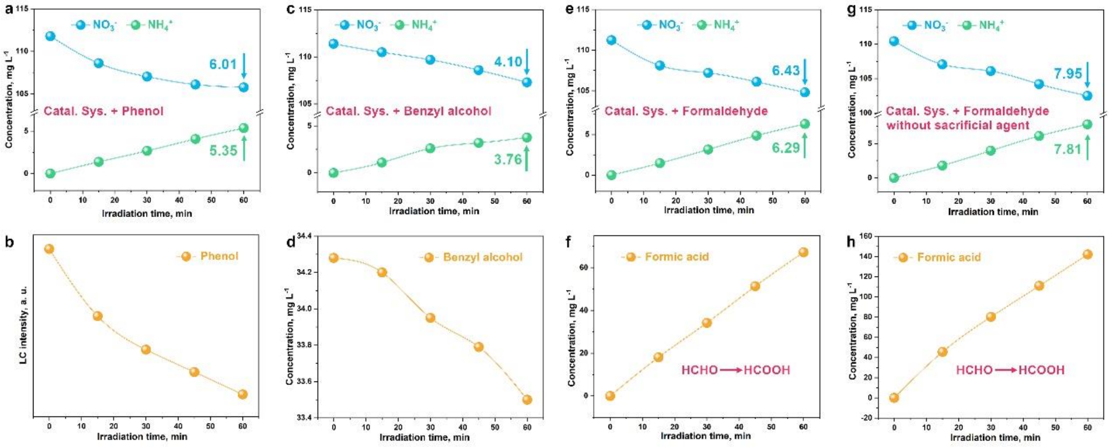

**Supplementary Figure 50.** Raw data of the efficiency evaluation in simulated wastewater containing the phenol (a, b), benzyl alcohol (c, d) and formaldehyde (e, f) as organic contaminants. The EG is excluded as hole sacrificial agent for the formaldehyde test (g ,h)

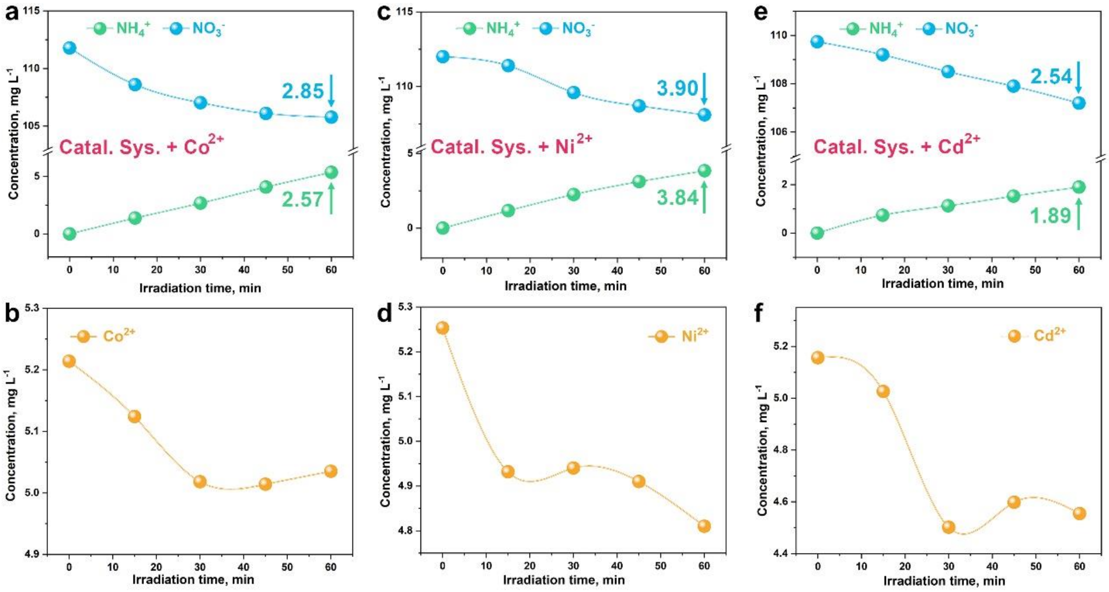

**Supplementary Figure 51.** Raw data of the efficiency evaluation in simulated wastewater containing the Co$^{2+}$ (a, b), Ni$^{2+}$ (c, d) and Cd$^{2+}$ (e, f) as cation contaminants.

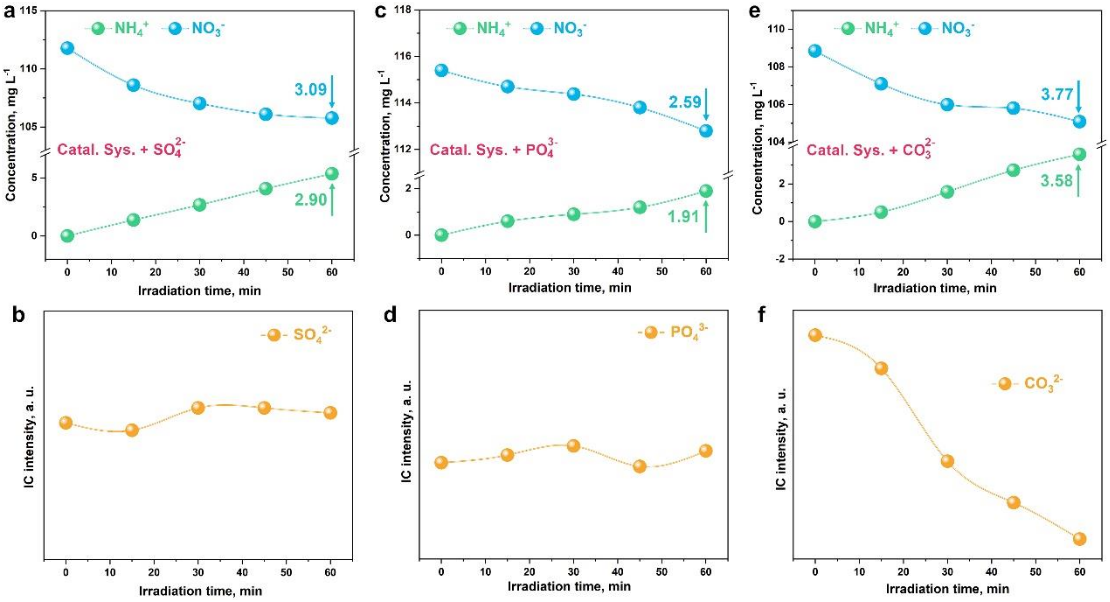

**Supplementary Figure 52.** Raw data of the efficiency evaluation in simulated wastewater containing the SO$_4^{2-}$ (a, b), PO$_4^{3-}$ (c, d) and CO$_3^{2-}$ (e, f) as anion contaminants.

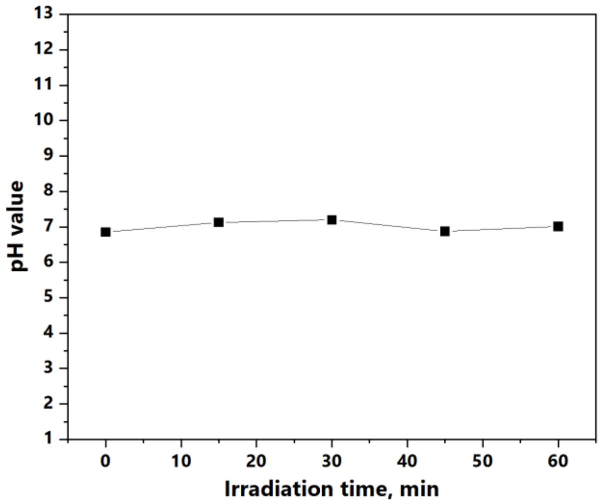

**Supplementary Figure 53.** pH value variation during the catalytic test.

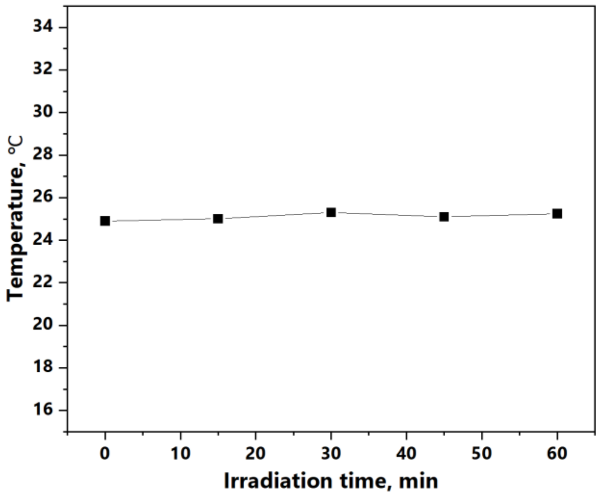

**Supplementary Figure 54.** Temperature variation during the catalytic test.

## Supplementary Note 1

### Apparent quantum yield calculation details

**●Photo flux calculation**

The photon flux in our photocatalysis measurements was obtained based on the following formulas:

$$\Theta = \frac{N}{ST}$$

$$\mathrm{N} = \frac{PT\ \bar{\lambda}}{hc}$$

$$\mathrm{P} = \bar{\mathrm{E}}\mathrm{S}$$

$$\bar{\lambda} = \frac{\int_{\Delta\lambda} \lambda E(\lambda) d\lambda}{E}$$

where Θ is the photo flux, *N* is the incident photon number, *S* stands for the illumination area of 3.0 $\mathrm{cm}^{-2}$, *T* refers to the illumination time, *h* corresponds to the Planck constant, c stands for the speed of light, $\lambda$ refers to wavelength, $\bar{\lambda}$ refers to an average wavelength (in this work the equivalent $\bar{\lambda}$ is 524.5 nm according to the MC-X301B light source used in this work, provided by the Merry Change Technology Co., Ltd.), $\bar{E}$ is the average optical power density measured by the optical power meter (74.6 mW $\mathrm{cm}^{-2}$), E is total radiation intensity, E(λ) is the spectrum radiation intensity. Thus, the photon flux Θ could be $1.97 \times 10^{17}\ \mathrm{s}^{-1}\ \mathrm{cm}^{-2}$.

**●Apparent quantum efficiency calculation**

The quantum efficiency is defined by the ratio of the effective electrons used for product formation to the total input photon flux. The reduction of $NO_3^-$ to $NH_4^+$ molecule requires eight electrons:

$$\mathrm{QE\%} = \frac{Effective\ electrons}{Total\ photons} \times 100\% = 8\mathrm{X}N/\Theta TS \times 100\%$$

where *X* is the yields of $NH_4^+$, respectively. *N* is Avogadro's number, *Θ* is the photon flux, *T* is the irradiation time, and *S* is the illumination area. The following calculation example is based on the data from $NO_3^-$RR with $\mathrm{BaO_{NCs}}$-TNS for 1h (Fig. 3a): $X=8.25\times10^{-3}$ mol, $N=6.022\times10^{23}\ \mathrm{mol}^{-1}$, $T=1$ h, $S=3.0\ \mathrm{cm}^2$; equivalent $\Theta=1.97\times10^{17}\ \mathrm{s}^{-1}\ \mathrm{cm}^{-2}$.

$QE\% = (8 \times 8.25\times10^{-3}\ \text{mol} \times 6.022\times10^{23}\ \text{mol}^{-1})/(1.97\times10^{17}\ \text{s}^{-1}\ \text{cm}^{-2} \times 1 \times 3600\ \text{s} \times 3.0\ \text{cm}^{2}) = 0.53\%$

**Supplementary Note 2**

Competing reaction pathways of $NO_3^-$ reduction for $NH_4^+$ photosynthesis (corresponding to the red line in Fig. 5c).

$$*NOH + {}^{\bullet}H \rightarrow *N + *H_2O \qquad (1)$$

$$*N + {}^{\bullet}H \rightarrow *NH \qquad (2)$$

$$*NH + {}^{\bullet}H \rightarrow *NH_2 \qquad (3)$$

$$*NH_2 + {}^{\bullet}H \rightarrow *NH_3 \qquad (4)$$

**Supplementary Note 3**

Potential side reaction pathways of $NO_3^-$ reduction into $N_2$ (corresponding to the purple and blue line in Fig. 5c).

$$*N + *N \rightarrow *N_2 \qquad (5)$$

**Supplementary Table 1** Comparison of the ammonia synthesis efficiency between $NO_3^-$RR to ammonia photosynthesis catalyzed by $BaO_{NCs}$ in this work and recently reported alkaline earth-based catalysts for ammonia synthesis.

| **Ammonia synthesis route** | **Catalyst** | **Optimal ammonia synthesis rate (mmol $g_{cat}^{-1}$ $h^{-1}$)** | **Reference** |
|---|---|---|---|
| **$NO_3^-$RR to ammonia Photosynthesis** | **$BaO_{NCs}$-TNS** | **89.79** | **This work** |
| Photocatalytic $N_2$RR to ammonia | BMOF(Sr)−0.2Fe | 0.78 | *ACS Catal.*, **2021**, *11*, 9986-9995. |
| Photocatalytic $N_2$RR to ammonia | g-$C_3N_4$/ $Mg_{1.1}Al_{0.3}Fe_{0.2}O_{1.7}$ | 0.27 | *RSC Adv.*, **2021**, *7*, 18099-18107. |
| Haber–Bosch process<br>$T$ = 360 °C<br>$P$ = 0.9 MPa | Ru/Ba-$Ca(NH_2)_2$ | 60.4 | *Angew. Chem. Int. Ed.*, **2018**, *57*, 2648-2652. |
| Haber–Bosch process<br>$T$ = 400 °C<br>$P$ = 10.0 MPa | Ba–Ru/CNTs-D | 49.0 | *J. Energy Chem.*, **2020**, *41*, 79-86. |
| Haber–Bosch process<br>$T$ = 340 °C<br>$P$ = 1.0 MPa | Ru/BaO-$CaH_2$ | 10.5 | *ACS Catal.*, **2018**, *8*, 10977-10984. |
| Haber–Bosch process<br>$T$ = 400 °C<br>$P$ = 0.1 MPa | Ru/$Sr_2Nb_2O_7$ | 4.98 | *Appl. Catal. A: Gen.*, **2018**, *554*, 1-9. |
| Haber–Bosch process<br>$T$ = 400 °C<br>$P$ = 0.1 MPa | Cs- Ru/$Sr_2Ta_2O_7$ | 5.04 | *J. Catal.*, **2020**, *389*, 556-565. |
| Haber–Bosch process<br>$T$ = 350 °C<br>$P$ = 0.9 MPa | Ru/$Ca(NH_2)_2$ | 31.7 | *ACS Catal.*, **2016**, *6*, 7577-7584. |
| Haber–Bosch process<br>$T$ = 340 °C<br>$P$ = 0.1 MPa | Ru-Cs/MgO | 1.65 | *ACS Catal.*, **2014**, *4*, 674-680. |
| Haber–Bosch process<br>$T$ = 300 °C<br>$P$ = 1.0 MPa | LiH/Co-Mg-O-co | 19 | *Chem. Comm.*, **2021**, *574*, 8576-8579. |
| Haber–Bosch process<br>$T$ = 400 °C<br>$P$ = 1.0 MPa | Ba–Ru/MgO | 25.2 | *J. Catal.*, **2003**, *214*, 327-335. |

**Supplementary Table 2** Comparison of the ammonia synthesis efficiency between $NO_3^-$RR to ammonia photosynthesis in this work and recently reported state-of-the-art ammonia synthesis routes under ambient conditions.

| **Ammonia synthesis route** | **Catalyst** | **Optimal ammonia synthesis rate (mmol $g_{cat}^{-1}$ $h^{-1}$)** | **Selectivity or Faraday efficiency (%)** | **long-term stability time (h)** | **Total ammonia synthesis yield (mmol)** | **Reference** |
|---|---|---|---|---|---|---|
| **$NO_3^-$RR to ammonia Photosynthesis** | **$BaO_{NCs}$-TNS** | **89.79** | **97.67** | **72** | **0.78** | **This work** |
| Photocatalytic $NO_3^-$RR to ammonia | JRC-TIO-6 | 0.016 | 97 | 24 | 0.384 | *ACS Catal.*, **2017**, *7*, 3713-3720. |
| Photocatalytic $NO_3^-$RR to ammonia | $Ag_2O$/P25 | 0.45 | 36.9 | 32 | 0.28 | *Appl. Catal. B: Environ.*, **2015**, *176-177*, 53-61. |
| Photocatalytic $NO_3^-$RR to ammonia | Au/$TiO_2$ | 0.69 | 39.0 | / | / | *Catal. Today*, **2012**, *181*, 171-176. |
| Photocatalytic $NO_3^-$RR to ammonia | PdSn/NiO/$NaTaO_3$ | 36 | 72 | / | / | *J. Catal.*, **2018**, *361*, 303-312. |
| Photocatalytic $N_2$RR to ammonia | OVs-$Bi_5O_7Br$ | 12.72 | / | 0.5 | 0.16 | *J. Am. Chem. Soc.*, **2020**, *142*, 12430-12439. |
| Photocatalytic $N_2$RR to ammonia | $K^+$@g-$C_3N_4$<br>With cyano groups | 3.42 | / | 4 | 0.14 | *Angew. Chem. Int. Ed.*, **2019**, *58*, 16644-16650. |

| | | | | | | |
|---|---|---|---|---|---|---|
| Photocatalytic $N_2$RR to ammonia | Etched ZnCr-LDH nanosheets | 0.03 | / | 3 | 0.003 | *Adv. Energy Mater.*, **2020**, *10*, 2002199. |
| Photocatalytic $N_2$RR to ammonia | $TiO_2$ nanosheets with oxygen vacancies | 0.08 | / | 3 | 0.005 | *Adv. Mater.*, **2019**, *31*, 1806482. |
| Photocatalytic $N_2$RR to ammonia | Au@UiO-66 | 0.81 | / | 24 | 0.29 | *J. Am. Chem. Soc.*, **2021**, *143*, 5727-5736. |
| Photocatalytic $N_2$RR to ammonia | Fe doped $TiO_2$ nanofibers | 0.06 | / | 8 | 0.0024 | *Angew. Chem. Int. Ed.*, **2021**, *60*, 16085-16092. |
| Photocatalytic $N_2$RR to ammonia | Al-PMOF (Fe) | 0.007 | / | 15 | 0.001 | *ACS Nano*, **2021**, *15*, 9670-9678. |
| Electrocatalytic $NO_3^-$RR to ammonia | Cu-PTCDA | 1.97 | 85.9 | 40 | 0.61 | *Nat. Energy*, **2020**, *5*, 605-613. |
| Electrocatalytic $NO_3^-$RR to ammonia | Pd nanocrystals | 3.611 | 35.1 | 4 | 0.002 | *ACS Catal.*, **2021**, *11*, 7568-7577. |
| Electrocatalytic $NO_3^-$RR to ammonia | Cu@Th-BPYDC | 1500 | 92.5 | / | / | *ACS Cent. Sci.*, **2021**, *7*, 1066-1072. |
| Electrocatalytic $NO_3^-$RR to ammonia | BCN@Cu | 576.2 | 88.9 | 20 | 2.30 | *J. Mater. Chem. A*, **2021**, *DOI: 10.1039/D1TA05718A*. |

| | | | | | | |
|---|---|---|---|---|---|---|
| Electrocatalytic $NO_3^-$RR to ammonia | Fe SAC | 1176 | 75 | 35 | 16.46 | *Nat. Commun.*, **2021**, *12*, 2870. |
| Electrocatalytic $NO_3^-$RR to ammonia | Cu-NBs-100 | 655 | 97% | 20 | 3.28 | *Energy Environ. Sci.*, **2021**, *14*, 4989-4997. |
| Electrocatalytic $NO_3^-$RR to ammonia | Strained Ru NCs | 5560 | 100 | 100 | 102.86 | *J. Am. Chem. Soc.*, **2020**, *142*, 7036-7046. |
| Electrocatalytic $N_2$RR to ammonia | PdCu-$TiO_2$ | 2.92 | / | 12 | 0.07 | *Nat. Chem.*, **2020**, *12*, 717-724. |
| Electrocatalytic $N_2$RR to ammonia | Bismuth nanocrystals | 200 | 66 | 50 | 0.52 | *Nat. Catal.*, **2019**, *2*, 448-456. |
| Electrocatalytic $N_2$RR to ammonia | Ru@$ZrO_2$/NC | 0.26 | 21 | 60 | 0.03 | *Chem*, **2019**, *5*, 204-214. |
| Electrocatalytic $N_2$RR to ammonia | $Fe_{SAs}$-$MoS_2$ | 36.1 | 31 | 50 | 9.025 | *Chem*, **2020**, *6*, 1-17. |
| Electrocatalytic $N_2$RR to ammonia | Cu-$TiO_2$ (OVs) | 1.52 | 21.99 | 12 | 0.04 | *Adv. Mater.*, **2020**, *32*, 2000299. |
| Electrocatalytic $N_2$RR to ammonia | CoPC NTs | 6.29 | 27.7 | 20 | 0.126 | *ACS Nano*, **2021**, *15*, 5230-5239 |

| | | | | | | |
|---|---|---|---|---|---|---|
| Electrocatalytic $N_2$RR to ammonia | Ru single atoms on N-doped carbon | 7.06 | 29.6 | 12 | 0.09 | *Adv. Mater.*, **2018**, *30*, 1803498. |
| Electrocatalytic $N_2$RR to ammonia | Black phosphorus nanosheets | 1.85 | 5.07 | 10 | 0.004 | *Angew. Chem. Int. Ed.*, **2019**, *58*, 2612-2616. |
| Electrocatalytic $N_2$RR to ammonia | Fe single-atoms on $MoS_2$ nanosheets | 0.51 | 18.8 | 12 | 0.02 | *Angew. Chem. Int. Ed.*, **2020**, *59*, 20411-20416. |
| Electrocatalytic $N_2$RR to ammonia | $Ti_3C_2T_x$ Mxene nanosheets | 0.16 | 5.78 | 12 | 0.0002 | *Joule.*, **2019**, *3*, 279-289. |
| Electrocatalytic $N_2$RR to ammonia | $Pd_{SAs}$-Cu NCs | 4.07 | 24.8 | 30 | 0.059 | *Angew. Chem. Int. Ed.*, **2020**, *60*, 345-350. |
| Electrocatalytic $N_2$RR to ammonia | Body-centered cubic PdCu nanoparticles | 2.10 | 11.5 | 10 | 0.004 | *Angew. Chem. Int. Ed.*, **2020**, *59*, 2649-2653. |
| Electrocatalytic $N_2$RR to ammonia | Pt/Au-ZIF | 9.47 | 44 | / | / | *Angew. Chem. Int. Ed.*, **2020**, *59*, 16997-17003. |
| Electrocatalytic $N_2$RR to ammonia | C doped $TiO_2$ | 0.87 | 17.8 | 11 | 0.006 | *Angew. Chem. Int. Ed.*, **2019**, *58*, 13101-13106. |
| Photoelectrochemical $N_2$RR to ammonia | Aerophilic-hydrophilic Au-Si heterostructures | / | 37.8 | 50 | 0.007 | *Chem*, **2020**, *5*, 617-633. |

| | | | | | | |
|---|---|---|---|---|---|---|
| Photoelectrochemical $N_2$RR to ammonia | Black phosphorus nanosheets | 6.02 | 23.3 | 12 | 0.007 | *Adv. Funct. Mater.*, **2020**, *30*, 2002731. |
| Photoelectrochemical $N_2$RR to ammonia | $Cu_2S$-$In_2S_3$ heterostructure | 2.78 | 33.3 | 24 | 0.033 | *J. Mater. Chem. A*, **2021**, *9*, 10497-10507. |
| Photoelectrochemical $N_2$RR to ammonia | $MoSe_2$-$C_3N_4$ heterostructure | 0.45 | 28.9 | 20 | 0.009 | *J. Mater. Chem. A*, **2021**, *9*, 2742-2753. |

**Supplementary Table 3** Source and purity of chemicals used in this work

| Chemicals | **Purity** | **Source** |
|---|---|---|
| Hydrofluoric Acid | 48%-50% | Adamas |
| Titanium(IV) butoxide | 99% | Adamas |
| Ethanol | 99.7% | Greagent |
| Potassium nitrate | 99.0% | Greagent |
| Magnesium chloride hexahydrate | 99% | Adamas |
| Calcium chloride hydrate | 99.0% | Acros |
| Strontium chloride hexahydrate | 99% | Adamas |
| Barium chloride dihydrate | 99.5% | Greagent |
| Phenol | ≥99.0% | Greagent |
| Benzyl alcohol | 99% | Adamas |
| Formaldehyde | 37.0%-40.0% | Greagent |
| Cobalt(II) chloride hexahydrate | 99% | Adamas |
| Nickel(II) chloride hexahydrate | 99% | Adamas |
| Cadmium chloride hydrate | 98% | Sigma-Aldrich |
| Potassium sulfate | ≥99.0% | Greagent |
| Potassium phosphate | 99% | Adamas |
| Potassium Carbonate | ≥99.0% | Greagent |